Research Article

Thermo-fluidic characteristics of an aerodynamic swirl nozzle with low-concentration nanofluids

MD Tanvir Khan[*, 1], Sudipta Debnath[2], Zahir U. Ahmed[2]

[1] *Department of Mechanical and System Engineering, Okayama University, Okayama – 700-8530, Japan*

[2] *Department of Mechanical Engineering, Khulna University of Engineering & Technology (KUET), Khulna – 9203, Bangladesh*

ABSTRACT

Anticipating the swirl turbulent flow and heat transfer phenomena within a nozzle is tremendously challenging due to the complexities of measurement diagnostics. The amalgamation of nanoparticles with fluids often exacerbates this perplexity for the resurgence of effective fluid properties that ambiguously affect thermo-fluidic behaviors. This study numerically focuses on the low concentration (1%) nanoparticles to investigate the effect of swirl as well as nanofluids on the flow and thermal characteristics of incompressible turbulent liquid jets. Both the aqueous and non-aqueous nanofluids are taken into consideration in a variety of flow conditions. The aqueous nanofluid resembles the properties of water, while the thermofluidic behavior of the non-aqueous nanofluids differs significantly. The Reynolds number enhances the average Nusselt number as well as the pressure drop inside the nozzle, and the non-aqueous nanofluids exhibit a relatively higher average Nusselt number and pressure drop. The average Nusselt number increases up to 322% for Dowtherm + Al_2O_3, and 320% for Syltherm800 + Al_2O_3 compared to H_2O. Aqueous nanofluid indicates a higher thermal performance factor than non-aqueous nanofluids. The skin friction coefficient decreases with the Reynolds number since the effective viscosity reduces. $(CH_2OH)_2$ + Al_2O_3 predicts the maximum heat transfer rate albeit with a penalty of high-pressure drop. Correlations are developed for the average Nusselt number and thermal performance factor to relate several control parameters.

1. Introduction

Swirl flows are highly complex in nature and have enormous engineering applications such as internal combustion engines, gas turbines, burners, chemical processing plants, rotary kilns, and spray dryers [1]. Due to the effect of angular momentum either a solid body rotation or free vortex flow emanates in the swirl flow. Tangential velocity increases with the radial distance in the case of a solid

---

Corresponding e-mail: tanvir.anik2196@gmail.com (MD Tanvir Khan)

Nomenclature

A	Nozzle area (1256.64 mm^2)	U_b	Bulk velocity (axial) (m/s)
C_μ	Eddy viscosity coefficient	W	Tangential velocity (m/s)
C_p	Specific heat (J/Kg.K)	W_b	Bulk velocity (tangential) (m/s)
D	Nozzle diameter (40 mm)	*Greek symbols*	
h	Heat transfer coefficient (W/m^{2}k)	μ	Viscosity (kg/ms)
k	Kinetic energy (m^2/s^2)	μ_t	Turbulent viscosity (kg/ms)
Nu	Nusselt number (hD/k)	μ_f	Viscosity of base fluid (kg/ms)
Pr	Prandtl number (dimensionless)	μ_{nf}	Viscosity of nanofluid (kg/ms)
ΔP	Pressure drop (kPa)	ρ	Density (kg/m^3)
Q_a	Axial inlet flow (Kg/s)	ρ_f	Density of base fluid (kg/m^3)
Q_r	Flow ratio	ρ_{nf}	Density of nanofluid (kg/m^3)
Q_t	Tangential inlet flow (Kg/s)	ρ_s	Density of solid particles (kg/m^3)
r	Nozzle radius (20 mm)	λ_f	Thermal conductivity of base fluid (W/m.k)
Re	Reynolds number (dimensionless)	λ_{nf}	Thermal conductivity of nanofluid (W/m.k)
S	Swirl number (W_b/U_b)	λ_s	Thermal conductivity of solid particles (W/m.k)
S^*	Local swirl number (W/U)	φ	Volume fraction of nanoparticle
U	Axial velocity (m/s)	η	Thermal performance factor (dimensionless)

body rotation while decreases for free vortex flow. Swirl can be generated in a number of ways such as axial-plus-tangential entry [2], rotating pipe [3], helical or twisted tape [4], rotating vane or perforated plate inside stationary pipe [5], ducted propeller [6], and so on. However, the aerodynamics of the associated flow embodies the common interesting behavior of rotating turbulence motion either in the case of non-isotropic free turbulence encountered in free jets or wake flows behind obstacles (for the geometry-induced swirl). The tangential velocity incorporated in swirl flow evolves the radial and axial pressure gradients which, in turn, affect the downstream free flow development as well as the wall-bounded flows. The adverse axial pressure gradient at high swirl flow is large enough to create a vortex breakdown that results in a reversed flow along the axis [7]. Existing swirl-associated research substantially focuses on the geometry-induced flow where the swirl is generated by a twisted tape insert or helical screw. The obvious drawback of such a system includes the lack of control over swirl intensity

and difficulty in flow regeneration due to strong dependency on geometrical accuracy. Moreover, in the case of swirl vanes, the flow is not found axisymmetric, and the flow field is complicated by additional secondary flows [8]. In contrast, an aerodynamic swirl generation system or axial-plus-tangential entry flow has the merit of not associating any geometry-induced flow reversal or trailing vortices as well as better control over the large domain of swirl intensity [9]. Both experimental investigation and numerical analysis on aerodynamically generated swirl flow have recently progressed alongside geometry-induced swirl flow in academic and industrial sections due to varieties of heating and cooling applications requiring faster heat transfer. However, fundamental flow characteristics inside an aerodynamic swirl nozzle are still not well understood. Nanofluid, on the other hand, has achieved increasing interest over the last couple of decades as an alternative means of accelerating heat transfer and thermal performance due to the high conductivity of nanoparticles compared to their base fluid [10]. The flow field is

significantly modified by dispersion, Brownian motion, and nanoparticle migration within the fluid, which leads to an increased convective heat transfer [11]. When nanofluid is associated with swirl flow, it greatly improves the momentum diffusion and turbulent eddy due to the swirling effect. As a result, the nanoparticles in the nanofluid become more dynamic and are expected to collide with fluid particles more frequently. This increases the effective heat transfer area, leading to a significant improvement in heat transfer performance. Hence nanofluids have been applied recently in a plethora of common engineering applications, such as pipe flows [12], helically coiled tubes [13], heat exchangers [14], solar collectors [15], thermosiphons [16], pulsating heat pipes [17]. In addition, the enhancement of nanoparticle volume fraction is believed to be a paramount parameter to ameliorate the heat transfer performance due to the effective thermal conductivity expansion [18]. However, with the increase of nanoparticle volume fraction, the effective viscosity of the fluid increases simultaneously, which in turn enhances the pressure drop [19] and friction factor [20]. Therefore, the pumping power as well as the operating cost becomes high. Besides, the higher volume concentration of nanoparticles also adversely affects the heat transfer performance [21] due to nanoparticle suspension and sedimentation. Thus, a small amount of nanoparticles with base fluid is beneficial for heat transfer augmentation, although this augmentation is indefinite and there exists a critical nanoparticle concentration, beyond which heat transfer performance is detrimental. This optimum or critical concentration in experimental studies varies within 0.01–10% [22-24]. Therefore, this study primarily focuses on examining low-concentration nanofluids (volume fraction, φ = 1%), subjected to an aerodynamically generated swirl flow.

A number of researches have been carried out and still continuing regarding swirling flow and nanofluid. Among the relevant research, Islam et al. [25] numerically investigated the effect of different nozzle parameters on flow behaviors and found that the axial velocity, static pressure, and turbulent kinetic energy strongly depend on the number of tangential ports. Moreover, the tapered conical shape nozzle uniformly predicts the turbulence but the curve shape nozzle exhibits very high turbulence. Halder et al. [26] experimentally studied the effect of flow and geometrical parameters on the conical nozzle shape and size and revealed that the air core diameter sharply increases with the inlet Reynolds number below 11,000. Promvonge and Eiamsa-Ard [27] found a significant enhancement in heat transfer rate by attaching a conical nozzle and swirl generator with a circular tube at a uniform heat flux condition. Singh and Ramamurthi [28] found an enhancement of swirl number with the Reynolds number for the laminar and turbulent flow conditions which eventually affect the formation of the wall-attached jet. Besides, the onset of two recirculation bubbles near the nozzle exit assists in the formation of a Coanda jet. Khan et al. [29] discovered that the swirl flow strongly affects the near-wall axial and tangential velocity. Moreover, turbulence characteristic at the onset of the swirl fluctuates abruptly and the swirl decay is almost constant after the nozzle converging section. Analyzing air jets numerically Guo et al. [30] found that the maximum axial velocity increases with axial distance and the peak of the tangential velocity at the wall vicinity reduces with the swirl decay. Heriz et al. [31] conducted a numerical analysis of swirl flow in a gas-liquid cylindrical cyclone separator for different numerical models and observed that the Realizable k–ε model anticipates the velocity profiles perfectly with the LES model in the case of a single tangential inlet swirl generation, while LES is found superior for multiple inlets. Upon comparing different turbulent models Najafi et al. [32] asserted that the two-equation models with different wall functions are pretty good at predicting the swirl behavior in solid body rotation regions. However, the RSM with a two-layer zone model is the best for near-wall treatment since it can focus the pressure distribution thoroughly along the pipe wall. Sentyabov et al. [33] studied different RANS models considering streamline curvature and detached

eddy simulation (DES) method and observed that the RANS models substantially regenerate the experimental data for low swirl flow. Escue and Cui [34] found an unsubstantial decay of the turbulence quantities immediately downstream of the inlet region while simulating swirl flow inside a smooth straight pipe. Saqr and Wahid [35] found that the swirl number radically affects the local entropy generation in a turbulent non-isothermal pipe flow due to viscous dissipation in the inner core of the Rankine vortex structure.

Regarding nanofluids, Akyürek et al. [36] found an improvement in the average Nusselt number with the nanoparticle volume fraction and Reynolds number although no significant change in pressure drop was observed for low nanoparticle concentrations. Kanti et al. [37] obtained an enhancement of the thermal performance factor with the nanoparticle concentration for the aqueous nanofluids. Reddy and Rao [38] observed that the heat transfer coefficient and friction factor enhanced by 10.73% and 8.73%, respectively, for 0.02% volume concentration of TiO_2 nanofluid when compared to base fluid flowing in a tube. Kahani et al. [39] achieved a higher heat transfer performance of aqueous Al_2O_3 than aqueous TiO_2 due to the greater thermal conductivity and low particle size of Al_2O_3. Moreover, the helical-coiled tube performs better than the straight tube in terms of heat transfer enhancement albeit with a penalty of increased pressure drop [40]. Heris et al. [41] observed that higher nanoparticle concentration and smaller nanoparticle size exhibit relatively higher heat transfer performance. Besides, flowing nanofluid through non-circular conduits has the benefits of low-pressure drop as well as a high Nusselt number compared to circular conduits [42]. Asmaie [47] obtained about 46 % greater maximum heat flux and 19.6 % reduction in average wall temperature using 0.1 to 1 wt.% concentration of aqueous CuO nanofluid while 1 wt.% was the optimum concentration. Choi and Zhang [44] developed a correlation of heat transfer enhancement with the Reynolds number, Prandtl number, specific heat, and volume concentration of nanofluids. Wanatasanappan et al. [45] evaluated the

effect of nanoparticle volume fraction on the effective viscosity and developed a correlation for the viscosity prediction. Behroyan et al. [46] investigated the laminar force convection performance of aqueous Al_2O_3 nanofluid for different numerical models in a heated tube and found that although both NSP (Newtonian Single-Phase) and non-NSP models under-predict Nusselt number, the non-NSP model showed a relatively better accuracy. Although the majority of the research achieved a heat transfer rate improvement in the nanofluid application, Meng and Li [47] and Shirvan et al. [48] observed a Nusselt number reduction with the nanoparticle volume fraction increment after a threshold value for the same Rayleigh number. This can be attributed to the fact that although a nanofluid with a higher concentration has higher effective thermal conductivity, it also induces more fluid viscosity which in turn reduces the flow speed as well as the heat transfer rate. Purohit et al. [49] found a reduction in entropy generation in the case of nanofluid compared to the base fluid for the same Reynolds number. Moreover, an enhancement in wall shear stress was also observed although negligible for an equal mass flow rate. Solomon et al. [50] found a significant reduction in the wall temperature, operating pressure, vapor temperature, and total resistance of the heat pipe by the application of an aqueous Cu nanofluid.

Although state-of-the-art research has been conducted on nanofluid in various aspects, remarkable studies on nanofluid-induced (aerodynamic) swirl flows have not been conducted yet. Investigations of thermo-fluidic behaviors for various nanofluid mediums are not been adequately addressed before and the impact of the base fluid and nanoparticle concentrations on the thermal and turbulence characteristics have not been understood properly. Moreover, aqueous nanofluids with low nanoparticle volume fraction exhibit the behavior of water since the properties are dominated by the base fluid [51]. Therefore, in this research, non-aqueous nanofluids are taken into consideration to conduct a numerical analysis by introducing swirl flow with nanofluids in an aerodynamic swirl nozzle. The heat transfer behavior and

the thermal performance of different nanofluids are investigated and their relative dependency on the nanofluid effective properties and flow parameters are discussed. Additionally, the result of this study may also be used as inlet boundary conditions of many swirl flow applications for the use of nanofluids as working mediums, such as impinging jets [52], combustors, and solar collectors. The nozzle has the flexibility of achieving from no swirl to high swirl for the same nozzle arrangement. The paper examines the effect of different non-aqueous nanofluids on the thermofluidic behaviors of an aerodynamic swirl nozzle. The nozzle outlet velocity profiles, average Nusselt number, pressure drop, thermal performance, local swirl behavior, and turbulent kinetic energy are investigated at isoflux (1000 W/m^2) conditions. The results are compared with the water and aqueous nanofluids for identical flow conditions. Moreover, the effect of different Reynolds numbers (Re = 5000, 11600, 24600, 35000), and the tangential nozzle flow/axial nozzle flow i.e. flow ratio (Qr = 0, 0.5, 1) are also discussed, and correlations are developed for average Nusselt number and thermal performance factors.

2. Methodology

An aerodynamic swirl nozzle is modeled based on the experimental setup of Thermofluids Laboratory, Edith Cowan University, Australia, to achieve pragmatic results. The detailed dimension of this nozzle is available in Ahmed et al. [9], hence is not repeated here for brevity. The nozzle has a converging truncated cone and a straight pipe, as well as three tangential ports with an internal diameter of 12 mm. A honeycomb model was employed to ensure the uniform flow. The base has an internal diameter of 50 mm, while the straight pipe has an internal diameter (D) of 40 mm. The total length of the nozzle is 577 mm. The axial and tangential flows mix downstream of the tangential inlets to create an aerodynamic swirl. The three-dimensional schematic view along with the grid generation is illustrated in Fig. 1. In this analysis, there is one difference compared to the nozzle used at Edith Cowan University.

Specifically, the axial ports with settling chambers that were used to achieve uniform flow are not included here. Instead, a uniform flow is applied directly at the base (bottom) of the nozzle in order to simplify the calculations and reduce computational costs.

In this study, the Reynolds-averaged Navier–Stokes (RANS) approach is applied to solve the governing equations, since the paper mainly focuses on time-mean behavior and does not examine time-variant turbulence behavior and vortical structure, in which case a more computationally intensive Large Eddy Simulation (LES) method is required for accurate predictions. Thus, the governing equations used for the incompressible three-dimensional steady-state turbulent air jets are the mass, momentum, and energy conservations, which are in indicial notations:

$$U_i = 0 \qquad (1)$$

$$\rho\left(U_i \frac{\partial U_i}{\partial x_i} + U_j \frac{\partial U_j}{\partial x_j}\right) = \frac{\partial P}{\partial x_i} + \frac{\partial}{\partial x_i}\left[\mu_{eff}\left(\frac{\partial U_i}{\partial x_j} + \frac{\partial U_j}{\partial x_i}\right) - \overline{\rho u'_i u'_j}\right] \qquad (2)$$

$$\frac{\partial(\rho e v_i)}{\partial x_i} = \frac{\partial}{\partial x_i}\left(\lambda \frac{\partial T}{\partial x_i}\right) \qquad (3)$$

Here, μ_{eff} is the effective viscosity of the fluid and is equal to the sum of molecular viscosity (μ) and eddy viscosity (μ_t). The term $\overline{u'_i u'_j}$ is unknown and called Reynolds stresses, which governs the turbulence. The Reynolds stress components within the term $\overline{u'_i u'_j}$ in Equation (2) are determined via mean velocity gradients by the Boussinesq hypothesis using turbulent (eddy) viscosity μ_t. The Boussinesq approximation is expressed as:

$$\overline{u'_i u'_j} = \frac{2}{3} k \delta_{ij} - \mu_t\left(\frac{\partial u_i}{\partial x_j} + \frac{\partial u_j}{\partial x_i}\right) \qquad (4)$$

where μ_t is considered as a function of turbulence kinetic energy (k) and turbulence dissipation rate (ε), which are determined via an appropriate turbulence model. In this research, the Realizable k-ε model proposed by Shih et al. [53], is chosen to model turbulence transport quantities: turbulence kinetic energy, k, and turbulence dissipation rate, ε. Over the past decade, the Realizable k-ε model has become popular in the CFD community due to its superior performance, when used for flows involving boundary layers in strong adverse

pressure gradients, streamwise curvature, and separation and recirculation zones. This model

significantly enhances the accuracy of predicted spreading rates for round jets.
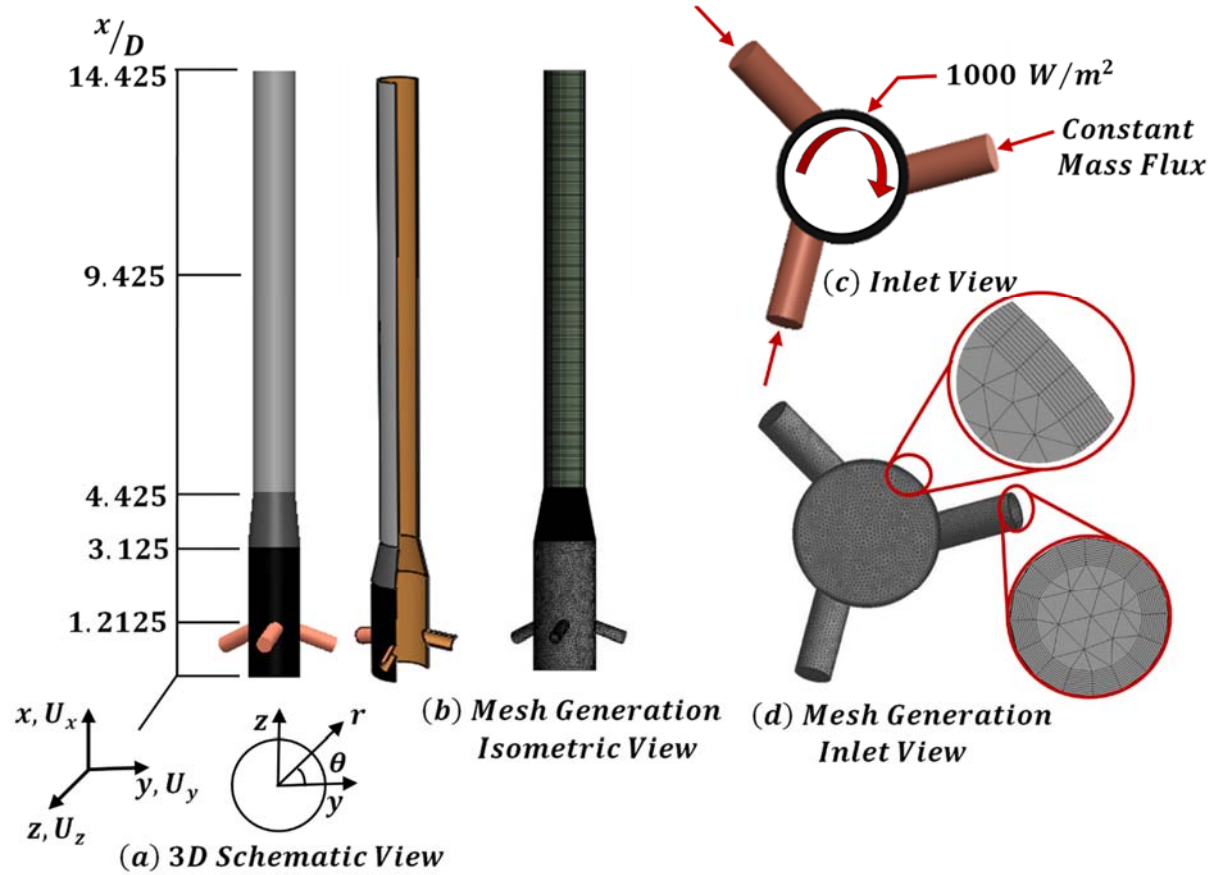

Fig. 1 (a) Three-dimensional view of an aerodynamic swirl nozzle; (b) Mesh generation (Isometric view); (c) Inlet view of the nozzle; (d) Mesh generation at inlet section with amplified view.

The Realizable k-ε model is defined by the following equations [54]:

$$\frac{\partial}{\partial x_j}\left(\rho k u_j\right) = \frac{\partial}{\partial x_j}\left[\left(\mu + \frac{\mu_t}{\sigma_k}\right)\frac{\partial k}{\partial x_j}\right] + P_k + P_b - \rho\varepsilon - Y_M + S_k \qquad (5)$$

$$\frac{\partial}{\partial x_j}\left(\rho\varepsilon u_j\right) = \frac{\partial}{\partial x_j}\left[\left(\mu + \frac{\mu_t}{\sigma_\varepsilon}\right)\frac{\partial \varepsilon}{\partial x_j}\right] + \rho C_1 S_\varepsilon - \rho C_2 \frac{\varepsilon^2}{k + \sqrt{\nu\varepsilon}} + C_{1\varepsilon}\frac{\varepsilon}{k}C_{3\varepsilon}P_b + S_\varepsilon \qquad (6)$$

where $C_1 = \max\left[0.43, \frac{\eta}{\eta+5}\right]$; $\eta = S\frac{k}{\varepsilon}$; $S = \sqrt{2S_{ij}S_{ij}}$.

Here, P_k represents the generation of turbulence kinetic energy due to the mean velocity gradients, and P_b is the generation of turbulence kinetic energy due to buoyancy.

Modelling Turbulent Viscosity:

$$\mu_t = \rho C_\mu \frac{k^2}{\varepsilon} \qquad (7)$$

$$C_\mu = \frac{1}{A_0 + A_s \frac{kU^*}{\varepsilon}}$$

where A_0 and A_s are model constants [54].

The above-governing equations and transport equations are solved numerically using ANSYS Fluent v17. The pressure-based coupled algorithm is chosen to solve the set of equations simultaneously. The pressure staggering option (PRESTO) is used for the pressure discretization and the second-order upwind discretization scheme is used for the convective terms. Mapped face meshing is applied at the nozzle outlet face, while multi-zone hexahedral meshing is used on the outer parts. Body sizing with an element size of 0.0025 m is utilized on the part containing tangential inlets. Ten inflation layers are employed with a first layer thickness of 0.0002 m and a growth rate of one to better-resolved

flow properties vicinity of the nozzle wall. Moreover, the 'Enhanced wall treatment' wall function is applied to precisely investigate the near wall features and the y+ value is found less than 0.2 for the whole computational domain. To examine the influence of grid size, four different grid elements are employed, namely, 974 k, 1310 k, 1647 k, and 1893 k cells. In this regard, the normalized axial velocity is plotted along the radial direction at the nozzle exit plane (x/D = 14.425). Fig. 2 represents the grid independence test for this analysis where identical results are obtained, except for 974 k nodes. As such, a mesh containing 1647 k element is chosen in this study. A converged solution is considered to be achieved when the residuals of the flow parameters are less than 10^{-5}.
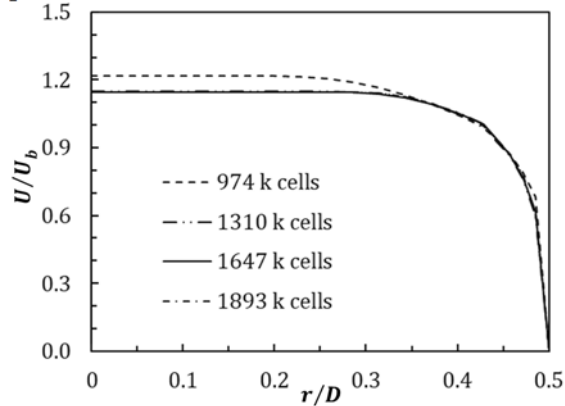

Fig. 2 Radial distribution of normalized axial (U/U$_b$) velocity of air at the nozzle outlet plane (x/D = 14.425) for different grids.

In this study, the nanoparticles dispersed into the base fluids are considered coolants and are assumed to be mixed homogenously with the base fluid. Usually, the large density difference between the nanoparticles and the base fluid is believed to be responsible for the sedimentation and agglomeration of nanoparticles over time. However, with proper nanofluid preparation techniques, sedimentation and agglomeration can be avoided, and a homogenous mixture can be obtained. Even if a small amount of nanoparticle coating somehow accumulates on the heat transfer surfaces, it is unlikely to affect the overall heat transfer behavior [55]. Additionally, since the nanoparticle

concentration is low in this study (φ = 1%) the impact of inter-particle interactions and aggregation is minimal. Thus the homogenous mixture of nanofluid assumption is valid and a suitable choice to investigate the thermofluidic behavior as well as to optimize the computational cost. Therefore, the nanofluids are considered to be single-phase fluids, and the classical theory of single-phase fluids is applied, where the physical properties of nanofluids are taken as a function of the properties of both constituents and their concentrations. The thermophysical properties of the nanofluids used in this study are calculated using the following equations [56-59]:

Density, $\rho_{nf} = (1- \varphi)\rho_f + \varphi\rho_s$ (8)

where φ = nanoparticle volume fraction, ρ_f = density of the base fluid (kg/m^3), ρ_s = density of the solid particles (kg/m^3).

Heat capacitance, $(\rho C_p)_{nf} = (1-\varphi) (\rho C_p)_f + \varphi(\rho C_p)_s$ (9)

where $(C_p)_f$ = heat capacitance of the base fluid (J/kg.K), $(C_p)_s$ = heat capacitance of the solid particles (J/kg.K).

Thermal expansion coefficient, $\beta_{nf} = (1-\varphi)\beta_f + \varphi\beta_s$ (10)

where β_f = thermal expansion coefficient of base fluid, β_s = thermal expansion coefficient of the solid particles.

Thermal diffusivity, $\alpha_{nf} = \lambda_{nf}/(\rho C_p)_{nf}$ (11)

where λ_{nf} = thermal conductivity of nanofluids (W/m.k).

Effective thermal conductivity,
$$\frac{\lambda_{nf}}{\lambda_f} = \frac{\lambda_s + 2\lambda_f - 2\varphi(\lambda_f - \lambda_s)}{K_s + 2\lambda_f + 2\varphi(\lambda_f - \lambda_s)}$$ (12)

where λ_f = thermal conductivity of base fluid (W/m.k), λ_s = thermal conductivity of solid particles (W/m.k).

Viscosity, $\mu_{nf} = \frac{\mu_f}{(1-\varphi)^{2.5}}$ (13)

where μ_f = viscosity of base fluid (kg/m.s).

The volume fraction of nanofluid is assumed 1% (φ = 1%). The properties of the base fluids and nanoparticles are presented in Table 1, and the properties of the nanofluids used in this analysis are listed in Table 2.

Table 1 Thermo-physical properties of pure water and nanoparticles at room temperature.

Properties	H_2O	Al_2O_3 [68]	$(CH_2OH)_2$ [69]	Dowtherm [70]	Syltherm800 [71]
ρ (kg/m³)	998.2	3880	1126	1056	930.64
C_p (J/kg.K)	4182	773	2354	1586.6	1616.66
K (W/m.K)	0.6	36	0.256	0.13624	0.13409
μ (kg/m.s)	0.001	-	0.021	0.00425	0.00853

Table 2 Thermo-physical properties of Nanofluids ($\varphi = 1\%$) at room temperature.

Properties	$H_2O+Al_2O_3$	$(CH_2OH)_2+Al_2O_3$	Dowtherm+Al_2O_3	Syltherm800+Al_2O_3
ρ (kg/m³)	1027.018	1153.54	1084.24	960.136
C_p (J/kg.K)	4053.21	2300.82	1598.396	1582.57
K (W/m.K)	0.6233	0.266	0.1417	0.1395
μ (kg/m.s)	0.001025	0.0215	0.0044	0.0087

For boundary conditions, mass flow inlets are used upstream of tangential ports (bottom of the nozzle) and through the tangential ports. Only the axial flow from the bottom of the nozzle is provided at the no-swirl conditions and no flows from tangential ports. In contrast, for the strongest swirl flows, only flows from tangential inlets are allowed to pass with no axial flow from the main inlet (bottom of the nozzle). For other proportions of axial-plus-tangential flows, intermediate swirl intensities are achieved. The total mass flow rates are directly calculated from the respective Reynolds numbers (see Table 3). The total mass flow rate is then divided into different proportions according to the flow ratio (Q_r) and applied to generate different swirl intensities. The flow ratio is the ratio of the total mass flow rate through tangential inlets to the total flow rates in the nozzle, i.e., the sum of flow rates through all axial and tangential inlets [29]:

$$Q_r = \frac{Q_t}{Q_a+Q_t} \qquad (14)$$

where Q_t = tangential inlet flow, Q_a = axial inlet flow.

The Reynolds number is defined as [29],

$$\text{Re} = \frac{Q_t D}{A v} \qquad (15)$$

where A is the nozzle area at the exit plane of the nozzle (1256.64 mm²), and ν is the dynamic viscosity of the fluid.

At the nozzle exit, atmospheric pressure is applied (Pressure outlet boundary conditions) whereby turbulence is specified by 2% intensity and hydraulic diameter. Finally, no-slip condition and 1000 W/m² heat flux condition are applied at the nozzle wall.

Table 3 Mass flow inlet conditions of different nanofluids ($\varphi = 1\%$) for different Reynolds numbers.

Nanofluids	Reynolds number (Re)	Total mass flow rate
H_2O	5000	0.157
	11600	0.364
	24600	0.773
	35000	1.3
$H_2O+Al_2O_3$	5000	0.161
	11600	0.374
	24600	0.792
	35000	1.1275
$(CH_2OH)_2+Al_2O_3$	5000	3.383
	11600	7.848
	24600	16.642
	35000	23.678
Dowtherm+Al_2O_3	5000	0.685
	11600	1.588
	24600	3.368
	35000	4.792
Syltherm800+Al_2O_3	5000	1.3741
	11600	3.188
	24600	6.761
	35000	9.62

In order to investigate the effect of different turbulent models on the predictability of suitable swirl generation, the flow velocity

8

near the nozzle outlet (x/D = 14.425) is illustrated in Fig. 3 for different turbulence models, namely, SST k-ω, Transition SST, SST CC, and Realizable k-ε. In this regard, the radial distribution of time-mean axial (U/U_b) and tangential (W/U_b) velocity profiles of air are plotted against the experimental data from previous literature [9] for Reynolds numbers, Re = 35000 at a medium swirl flow. Since much experimental analysis of nanofluid in aerodynamic swirl nozzle has not been conducted yet, therefore, the experimental data of air is used for the comparison. The

experimental data was acquired by X-wire CTA measurement for medium swirling air jets (S = 0.33) at 1 mm above the nozzle exit plane. It appears that the velocity profiles for all the turbulent models match the experimental data suitably in terms of trends and magnitudes, although the prediction of the Realizable k-ε model seems to have a superiority over the others. As a consequence, the present study has implemented the Realizable k-ε turbulent model for the rest of the analysis.
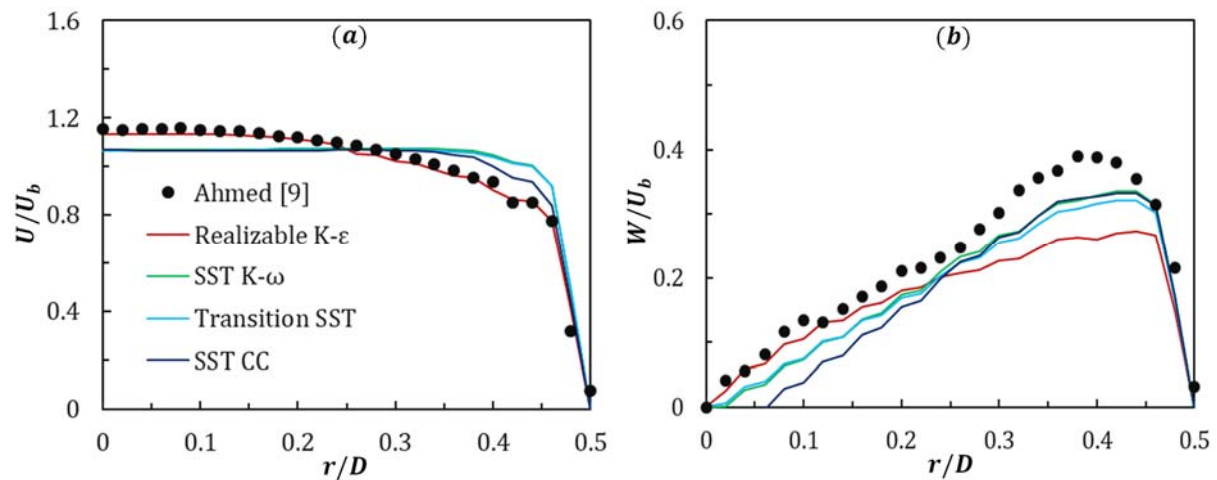

Fig. 3 Radial distribution of normalized (a) axial (U/U_b), and (b) tangential (W/U_b) velocity of air at the nozzle outlet plane (x/D = 14.425) for different turbulent models at medium swirl condition (Q_r = 0.5) and Reynolds number 35000 along with the corresponding experimental data.

Fig. 4 depicts the circumferentially averaged surface heat transfer coefficient to examine the presence of any circumferential non-uniformity at different axial locations of the nozzle. In this regard, the predicted surface heat transfer coefficient of H_2O + Al_2O_3 nanofluid (φ = 1%) was considered at four distinct axial positions (x/D = 5.77, 8.665, 11.54, 14.425), encompassing eighteen individual points around the nozzle periphery for the strongest swirl condition (Q_r = 1) at Re = 11,600 and wall heat flux 1000 W/m². A maximum 0.6% deviation for the local surface heat transfer coefficient (h) values is found from the circumferentially mean surface heat transfer coefficients. As such, the mean flow is expected to be uniform circumferentially at any particular axial location.
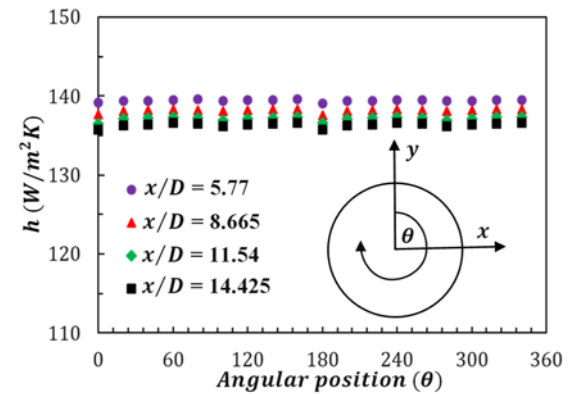

Fig. 4 Circumferential distributions of surface heat transfer coefficient at different axial locations of the nozzle.

3. Result & Discussion

3.1 Nozzle exit velocity distribution

Fig. 5 illustrates the radial distributions of normalized axial and tangential velocity

profiles of different nanofluids (φ = 1%) and a base fluid (water) at a Reynolds number 11600 at the nozzle exit plane (x/D = 14.425) for an identical mass flow rate of both the non-swirling and swirling flows along with the corresponding data of existing literature [51]. The normalization is done by dividing the axial and tangential velocities with the corresponding bulk velocities of the flow, which is defined as the total volumetric flow rate divided by the nozzle exit area. A uniformity in both the axial and tangential velocity profile is obtained for no swirl to high swirl cases in this analysis, which bolsters the accuracy of the numerical model. Although, for medium swirl condition (Q_r = 0.5) an over-prediction in the tangential velocity is observed for Dowtherm + Al_2O_3 near the center of the nozzle, however, for the other cases the velocity distribution is nearly the same. It is also observed that the water and aqueous nanofluids exhibit identical velocity profiles. For no swirl cases, the present analysis slightly under-predicts the axial velocities near the nozzle wall with the existing literature data. In the case of high swirl condition (Q_r = 1), monotonous anticipation is observed in both the axial and tangential velocity profiles. Therefore, although the Reynolds stress model (RSM) achieved the peak in the velocity distributions properly [51], however, uniformity in the overall velocity distribution can be obtained by the Realizable k-epsilon model. A deviation in the tangential velocity profiles is observed at Reynolds number 5000 for both the medium and high swirl condition in the case of Dowtherm + Al_2O_3, in which the near wall (*r/D* ≈ 0.30.47) tangential velocity is over-predicted (Q_r = 0.5) and under-predicted (Q_r = 1), respectively [Fig. A1]. Moreover, the axial velocity near the nozzle center is slightly higher than the other nanofluids for the strongest swirl case (Q_r = 1) and becomes lower at the near wall zone, which indicates low swirl generation. In the case of Reynolds numbers 24600 and 35000, Dowtherm + Al_2O_3 under-predicts the tangential velocities compared to the other nanofluids for the medium swirl cases (Q_r = 0.5), where the

other nanofluids exhibit almost identical velocity distribution [Fig. A2 and Fig. A3].

3.2 Average Nusselt number

Fig. 6 represents the variation of the average Nusselt number for different Reynolds numbers at the nozzle exit plane (x/D = 14.425) for different nanofluids (φ = 1%) and a base fluid (water). It is observed that the average Nussetl number is increasing with the Reynolds number for all the nanofluids, which can be attributed to the fact of increasing the flow velocity inside the nozzle which assists in rapid heat transfer. However, the average Nusselt number of $(CH_2OH)_2$ + Al_2O_3 is much higher than the other nanofluids, and a significantly high average Nusselt number is observed for higher Reynolds numbers. This might be due to the high effective thermal conductivity of the $(CH_2OH)_2$ + Al_2O_3 as well as better nanoparticle dispersibility in Ethylene glycol $(CH_2OH)_2$ [60]. The average Nusselt number accelerates with the increment of swirl intensity which ensures the proper mixing of nanoparticles for turbulence. Due to swirl turbulent flow, the fluid particles collide with each other which enhances the velocity as well as the heat transfer rate. The proper effect of swirl intensity is evident in the case of $(CH_2OH)_2$ + Al_2O_3 nanofluid where the average Nusselt number increases up to 52% from no swirl to high swirl condition, while other nanofluids exhibit a maximum of 8% (Dowtherm + Al_2O_3) enhancement. Besides, the H_2O and H_2O + Al_2O_3 exhibit identical characteristics in average Nusselt number distribution, which is also observed in a previous study [51]. In the case of Syltherm800 + Al_2O_3 and Dowtherm + Al_2O_3, a sharp increase in the average Nusselt number distribution is observed from Reynolds number 5000 to 11600, although for higher Reynolds numbers this increment trend is relatively smooth. The non-aqueous nanofluids show a higher average Nusselt number than the aqueous nanofluids from no swirl to high swirl cases, which is attributed to the fact of higher effective thermal conductivity as well as the proper swirl turbulence effect. The average Nusselt number increases up to 322% for Dowtherm + Al_2O_3 and 320% for

Syltherm800 + Al_2O_3 compared to H_2O. Such a high Nusselt number increment is plausible since this type of increment is found in previous studies, even if in the case of water-based nanofluids. For example, Ding et al. [61] obtained a maximum heat transfer enhancement over 350% using aqueous suspensions of carbon nanotubes (CNT nanofluids). Besides, Putra et al. [62] also observed 350% and 150% increments in heat transfer using CuO and Al_2O_3 nanofluid, respectively.
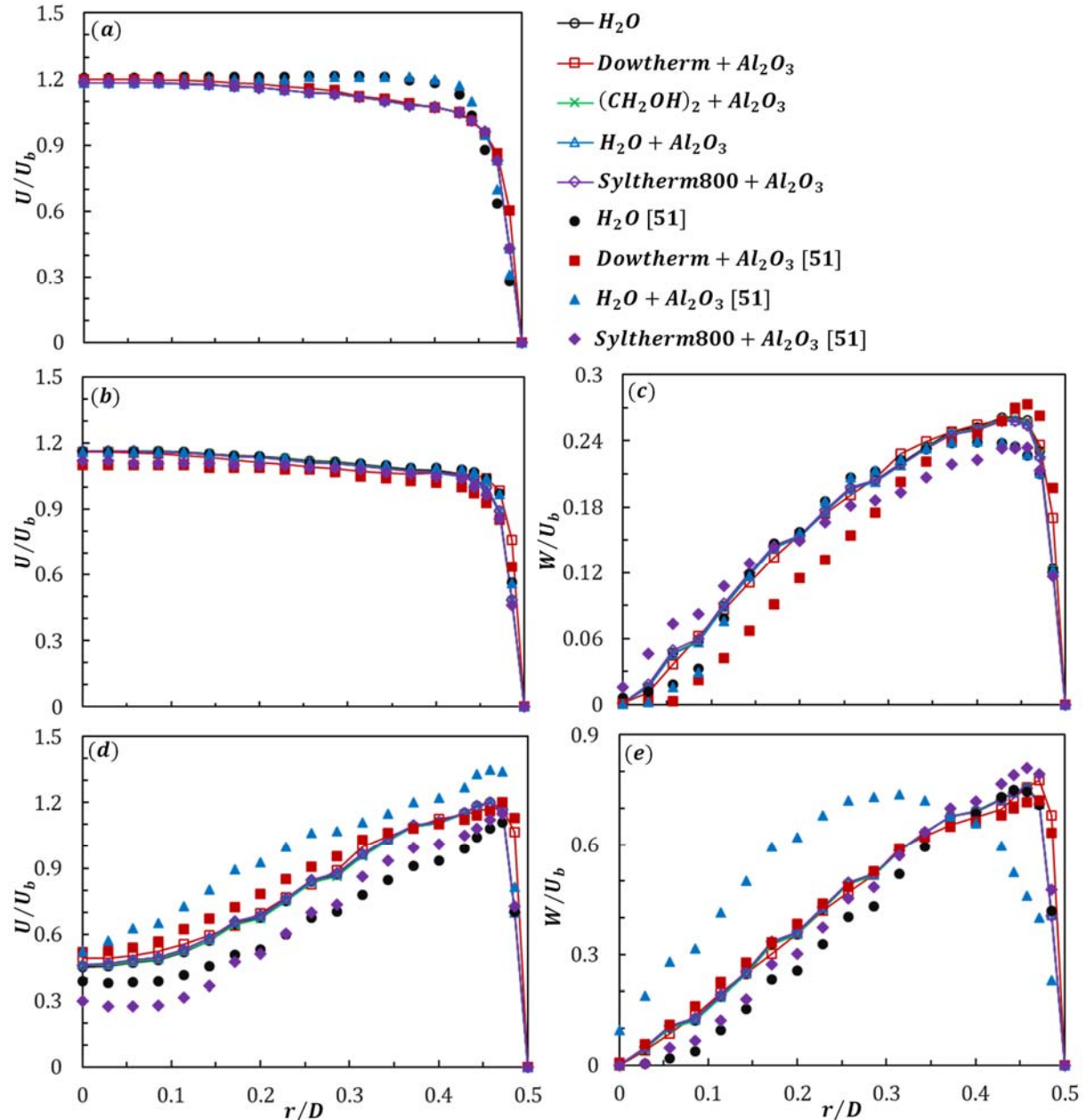

Fig. 5 Radial distributions of normalised (a), (b), (d) axial (U/U_b) and (c), (e) tangential (W/U_b) velocities of different nanofluids ($\varphi = 1\%$) along with water at the nozzle exit plane (x/D = 14.425) for Re = 11,600 at: (a) $Q_r = 0$, (b), (c) $Q_r = 0.5$, and (d), (e) $Q_r = 1$.
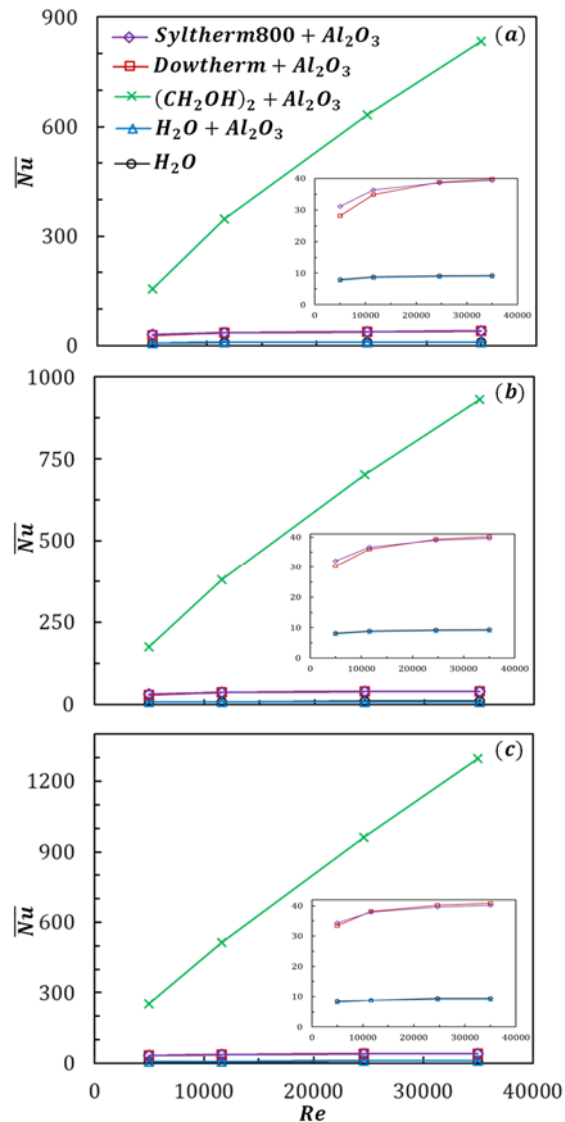
Fig. 6 Average Nusselt number distributions of pure water and different nanofluids ($\varphi = 1\%$) for different Reynolds numbers at (a) $Q_r = 0$, (b) $Q_r = 0.5$, and (c) $Q_r = 1$.

3.3 Nozzle interior pressure drop

Fig. 7 depicts the variation of pressure drop inside the nozzle of pure water and different nanofluids ($\varphi = 1\%$) for different Reynolds numbers. The pressure drop is calculated from the difference of static pressure between the nozzle inlet (x/D = 1.2125) and exit (x/D = 14.425). It is observed that the pressure drop of all the fluids increases with the Reynolds number. This can be attributed due to the fact of increased mass flow rate in the nozzle proportionally with the Reynolds number. When more mass flows

through a point in unit time then the force exerted by the mass molecules will be greater on the surface of the section, hence pressure will be more. Therefore, static pressure becomes more at the nozzle interior when the Reynolds number as well as the mass flow rate increases. However, the increment of static pressure at the nozzle inlet is greater than the nozzle exit, which eventually accelerates the pressure difference. Consequently, the pressure drop increases with the Reynolds number. It is also observed that the water and aqueous nanofluid exhibit the same pressure drop characteristics which is the lowest among the nanofluids. Moreover, the pressure drop of Syltherm800 + Al_2O_3 is greater than the Dowtherm + Al_2O_3, which is significantly high for $(CH_2OH)_2$ + Al_2O_3, especially at higher Reynolds numbers. This is because of the highly effective viscosity [0.0215 (*kg/m.s*)] of the $(CH_2OH)_2$ + Al_2O_3 nanofluid. In fact, the pressure drop is directly proportional to the effective viscosity of the nanofluids since the stickiness of the fluid increases with viscosity which results in high friction with the nozzle wall. Kanti et al. [63] also observed the same pressure drop behavior for the aqueous nanofluids. Thus, the pressure drop is influenced by the nanofluid effective viscosity.

3.4 Thermal performance factor

Fig. 8 delineates the thermal performance factor (η) distribution of different nanofluids ($\varphi = 1\%$) for different Reynolds numbers. The thermal performance factor is the efficiency calculating parameter in the case of nanofluid application. When nanofluids are utilized instead of base fluid, the heat transfer rate augments due to the increased effective thermal conductivity. Simultaneously the pressure drop also increases for the increased effective viscosity of the nanofluids, which eventually enhances the pumping power as well as the operating cost. Therefore, efficiency calculation is very important for the practical applications of such nanofluids. The thermal performance factor is calculated by the ratio of the relative average Nusselt number to the relative pressure drop [51],
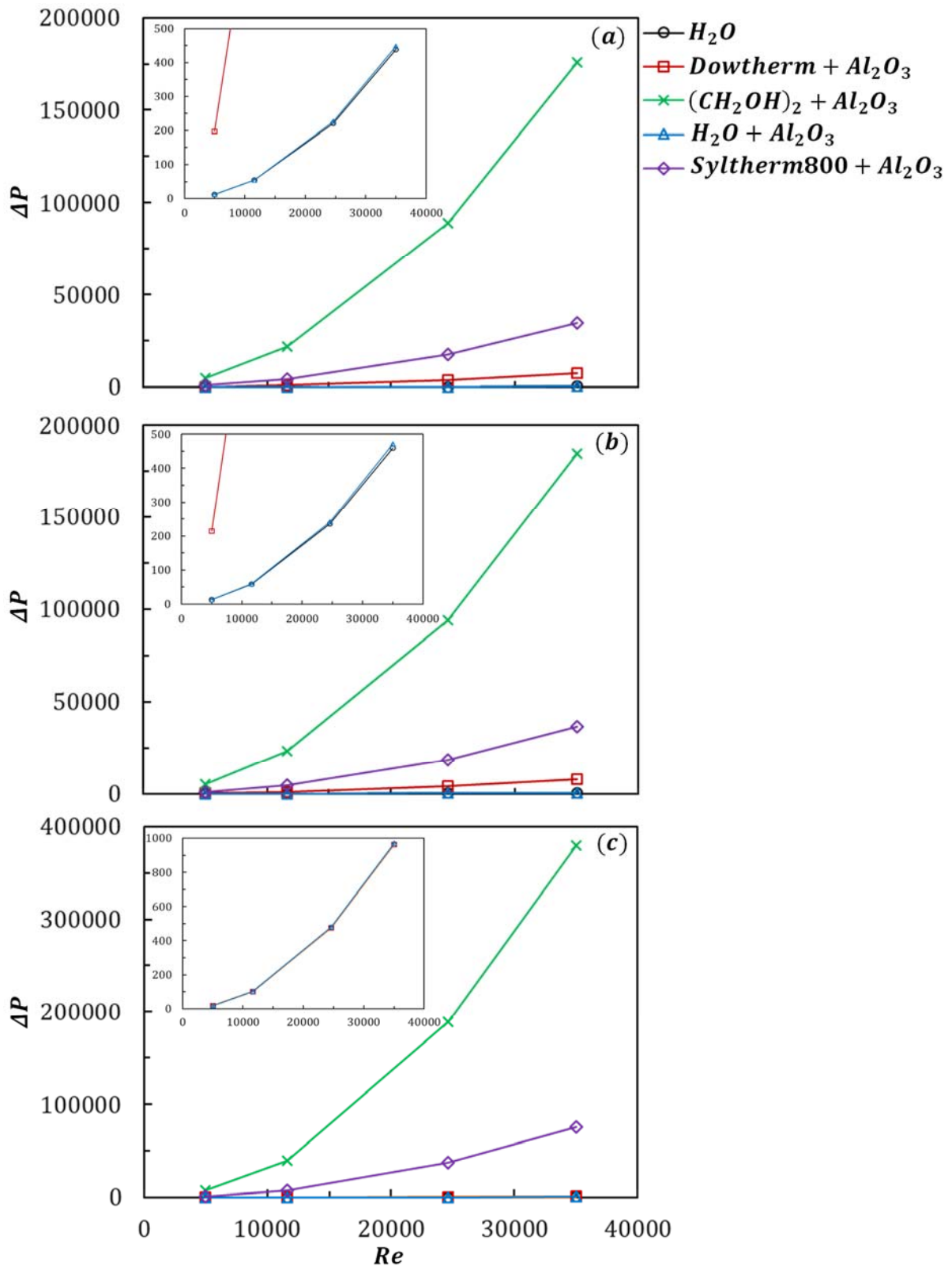
Fig. 7 Pressure drops of pure water and different nanofluids ($\varphi = 1\%$) inside the nozzle for different Reynolds numbers at (a) $Q_r = 0$, (b) $Q_r = 0.5$, and (c) $Q_r = 1$.

$$\eta = \frac{\frac{\overline{Nu}}{\overline{Nu}_{H_2O}}}{\frac{\Delta P}{\Delta P_{H_2O}}} \quad (16)$$

It is observed that the thermal performance factor is nearly constant for different Reynolds numbers and swirl conditions for water and almost all the nanofluids except $(CH_2OH)_2 + Al_2O_3$. In the case of $(CH_2OH)_2 + Al_2O_3$, the thermal performance factor is increasing with the Reynolds number. This might be due to the strong turbulence inside the nozzle at high flow velocity that assists the proper mixing of the base fluid and nanoparticles. Consequently, the nanofluid effective property especially the effective thermal conductivity increases which along with the high flow velocity results in a high convective heat transfer rate. Thus the relative average Nusselt number (the numerator in equation 16) increases comparatively higher than the relative pressure drop and as a consequence, the thermal performance factor increases with the Reynolds number. It is also observed that the aqueous nanofluid exhibits higher thermal performance than the other nanofluids which is due to the high effective thermal conductivity as well as low viscosity of water. Moreover, despite the same thermal conductivity, the Dowtherm + Al_2O_3 has a greater thermal performance factor than the Syltherm800 + Al_2O_3 since Syltherm800 + Al_2O_3 has higher effective viscosity which accelerates the pressure drop.

3.5 Correlations for average Nusselt number and thermal performance factor

The average Nusselt number $(\overline{Nu})$ and thermal performance factor (η), calculated from the numerical data, are used to develop correlations for the effect of flow variables and effective properties of the nanofluids relative to water (H_2O), such as Re, ρ/ρ_0, λ/λ_0, μ/μ_0. The correlations are established by multivariate regression analysis applying IBM SPSS, where the average Nusselt number $(\overline{Nu})$ and thermal performance factor (η) are considered as dependent variables, while Re, ρ/ρ_0, λ/λ_0, μ/μ_0 are considered as independent variables. Previous studies also

established analogous correlations using multivariate regression analysis [64, 65]. The resultant $\overline{Nu}$ and η correlations for both non-swirling and swirling jet arrays are given as follows:

$$\left.\begin{array}{l}\overline{Nu} = 0.002 Re^{0.814}\left(\frac{\rho}{\rho_0}\right)^{7.042}\left(\frac{\lambda}{\lambda_0}\right)^{0.555}\left(\frac{\mu}{\mu_0}\right)^{1.279}\\ \eta = 0.643 Re^{0.015}\left(\frac{\rho}{\rho_0}\right)^{7.688}\left(\frac{\lambda}{\lambda_0}\right)^{0.440}\left(\frac{\mu}{\mu_0}\right)^{-0.801}\end{array}\right\} Q_r = 0 \quad (17)$$

$$\left.\begin{array}{l}\overline{Nu} = 0.002 Re^{0.822}\left(\frac{\rho}{\rho_0}\right)^{7.296}\left(\frac{\lambda}{\lambda_0}\right)^{0.589}\left(\frac{\mu}{\mu_0}\right)^{1.312}\\ \eta = 0.631 Re^{0.016}\left(\frac{\rho}{\rho_0}\right)^{7.987}\left(\frac{\lambda}{\lambda_0}\right)^{0.462}\left(\frac{\mu}{\mu_0}\right)^{-0.773}\end{array}\right\} Q_r = 0.5 \quad (18)$$
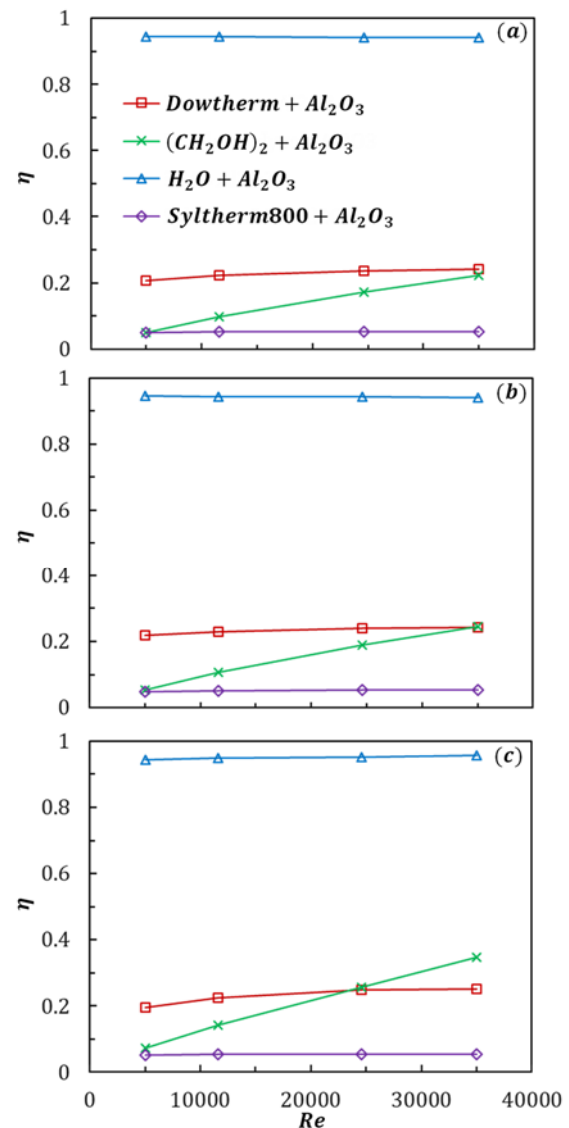

Fig. 8 Thermal performance factors of different nanofluids ($\varphi = 1\%$) for different Reynolds numbers at (a) $Q_r = 0$, (b) $Q_r = 0.5$, and (c) $Q_r = 1$.

$$\left.\begin{array}{l}\overline{Nu} = 0.001 Re^{0.837}\left(\rho/\rho_0\right)^{7.970}\left(\lambda/\lambda_0\right)^{0.712}\left(\mu/\mu_0\right)^{1.422} \\ \eta = 0.488 Re^{0.042}\left(\rho/\rho_0\right)^{8.466}\left(\lambda/\lambda_0\right)^{0.622}\left(\mu/\mu_0\right)^{-0.643}\end{array}\right\} Q_r = 1 \quad (19)$$

Where, Re, ρ/ρ_0, λ/λ_0, μ/μ_0 represent the Reynolds number, normalized density, normalized thermal conductivity, and normalized viscosity of the nanofluids, respectively. The normalization is done by the corresponding properties of water (H_2O).

Fig. 9 portrays the comparison between the computed values and the correlations with ±10% error bands. It appears that the majority of the data falls within these error bands. The R^2 value for the $\overline{Nu}$ correlation is found to be 0.998, 0.998, and 0.999; and the η correlation is found to be 0.991, 0.989, and 0.978 for the non-swirling, medium swirling, and swirling jets, respectively.
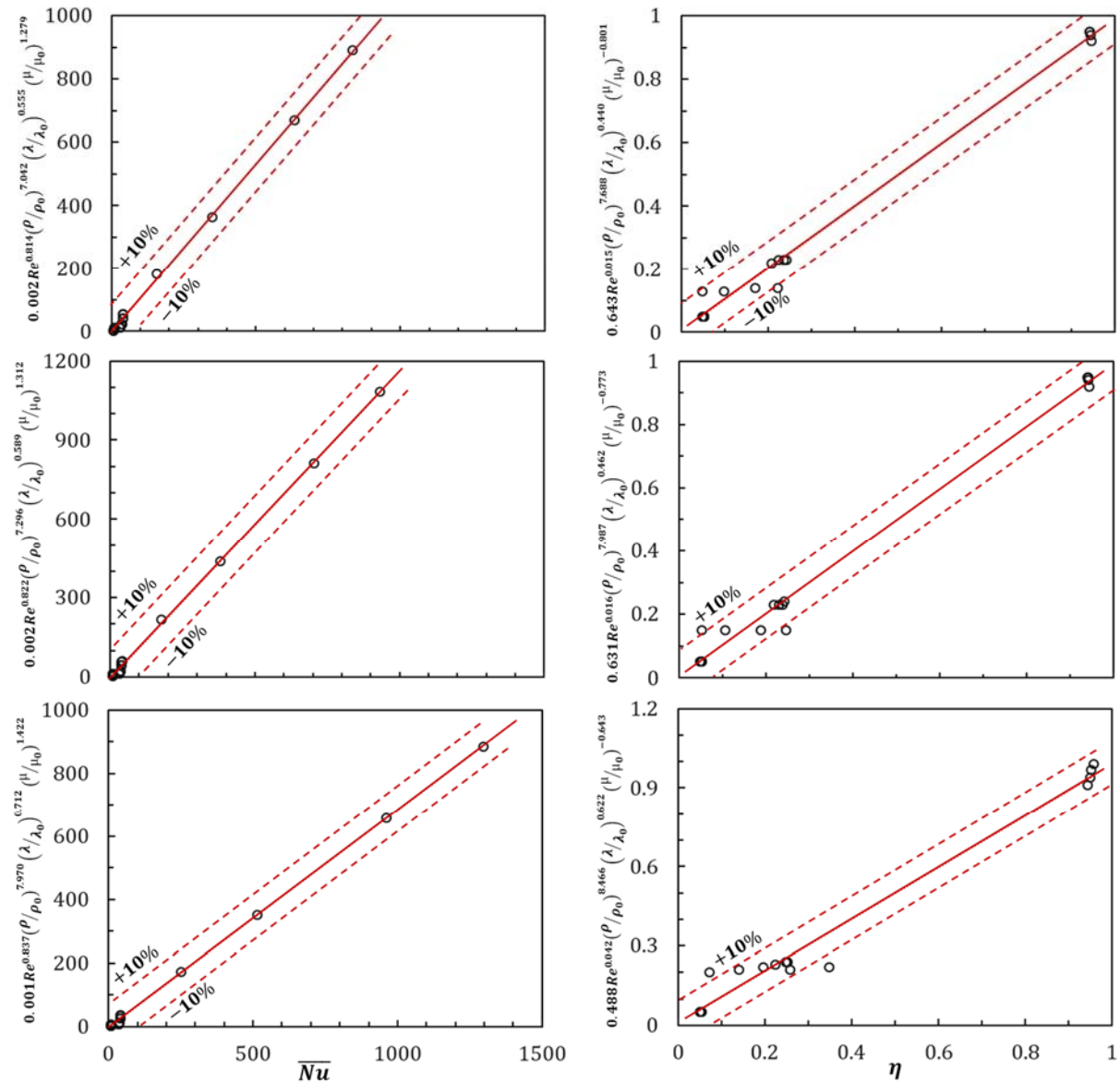

Fig. 9 Comparison between the numerical data and the value from the correlation for the average Nusselt numbers ($\overline{Nu}$): (a) $Q_r = 0$; (c) $Q_r = 0.5$; (e) $Q_r = 1$; and Thermal performance factors (η): (b) $Q_r = 0$; (d) $Q_r = 0.5$; (f) $Q_r = 1$. The figure also shows the ±10% error bands.

Moreover, another set of correlations is established in which the average Nusselt number is presented as a function of the Reynolds number and Prandtl number for water and other nanofluids from no swirl to high swirl conditions. The correlations are presented in Table 4. The R^2 value for the $\overline{Nu}$ correlation is found in the range of 0.944 to 1.0.

Table 4 Expression of average Nusselt number of water and different nanofluids ($\varphi = 1\%$) as a function of Reynolds number and Prandtl number for different swirl conditions.

Fluids	$Q_r = 0$	$Q_r = 0.5$	$Q_r = 1$
H$_2$O	$\overline{Nu} = Re^{0.077}Pr^{0.74}$	$\overline{Nu} = Re^{0.077}Pr^{0.79}$	$\overline{Nu} = Re^{0.077}Pr^{0.85}$
H$_2$O+Al$_2$O$_3$	$\overline{Nu} = Re^{0.077}Pr^{0.75}$	$\overline{Nu} = Re^{0.077}Pr^{0.79}$	$\overline{Nu} = Re^{0.077}Pr^{0.88}$
(CH$_2$OH)$_2$+Al$_2$O$_3$	$\overline{Nu} = Re^{0.077}Pr^{-0.35}$	$\overline{Nu} = Re^{0.077}Pr^{-0.35}$	$\overline{Nu} = Re^{0.077}Pr^{-0.31}$
Dowtherm+Al$_2$O$_3$	$\overline{Nu} = Re^{0.077}Pr^{0.49}$	$\overline{Nu} = Re^{0.077}Pr^{0.58}$	$\overline{Nu} = Re^{0.077}Pr^{0.69}$
Syltherm800+Al$_2$O$_3$	$\overline{Nu} = Re^{0.077}Pr^{0.54}$	$\overline{Nu} = Re^{0.077}Pr^{0.56}$	$\overline{Nu} = Re^{0.077}Pr^{0.63}$

3.6 Nozzle exit local swirl

Fig. 10 elucidates the local swirl behavior of water and different nanofluids ($\varphi = 1\%$) at the nozzle exit plane (x/D = 14.425). The local swirl number at the nozzle exit plane is very important since the nozzle-emanated fluid can be directly applied to impinging jets [66, 67] and numerous engineering applications. The local swirl number is defined as the ratio of tangential velocity to the axial velocity at a certain point [29],

$$S^*(r) = \frac{W}{U} \qquad (20)$$

where W = tangential velocity (m/s), and U = axial velocity (m/s)

It is observed that all the fluids show almost identical local swirl behavior at medium swirl cases for all the Reynolds numbers. However, for high swirl cases, the local swirl is increasing with the Reynolds numbers. This might be due to the fact that the increased velocity dominates over the viscosity for high swirl cases which accelerates the local swirl characteristics.

3.7 Skin friction coefficient

Fig. 11 epitomizes the axial distribution of the skin friction coefficient for water and different nanofluids ($\varphi = 1\%$) for different Reynolds numbers and swirl conditions. The skin friction coefficient is calculated by averaging the data from the different radial locations so that more accurate results can be predicted. It is observed that the skin friction coefficients at no swirl ($Q_r = 0$) and medium swirl ($Q_r = 0.5$) flow exhibit the same behavior for all the nanofluids and are comparatively lower than for high swirl ($Q_r = 1$) cases. Although for high Reynolds numbers the skin friction coefficient is identical for all the fluids, however, for low Reynolds numbers a non-uniformity is observed among the fluids, especially at Re = 5000. Moreover, the skin friction coefficient near the nozzle inlet section is higher than the nozzle exits and with the increment of axial distance, the skin friction coefficient is gradually decreasing for all the nanofluids. Besides, the magnitude of the skin friction coefficient near the nozzle inlet decreases with increasing Reynolds number for the high swirl cases. This might be due to the fact that the fluid viscosity that induces the skin friction coefficient is inversely proportional to the Reynolds number. When the Reynolds number is increased, the inertial forces become more dominant compared to the viscous forces which in consequence decreases the boundary layer thickness surrounding the nozzle wall. A thinner boundary layer results in a steeper near-wall velocity gradient and abrupt variation in velocity distribution which leads to a reduction in the effective viscosity of the fluid. Therefore, with the increment of Reynolds number the viscosity, as well as the skin friction coefficient, decreases. This behavior is more intense in the case of strong swirl conditions since the increased turbulence also assists in reducing friction.
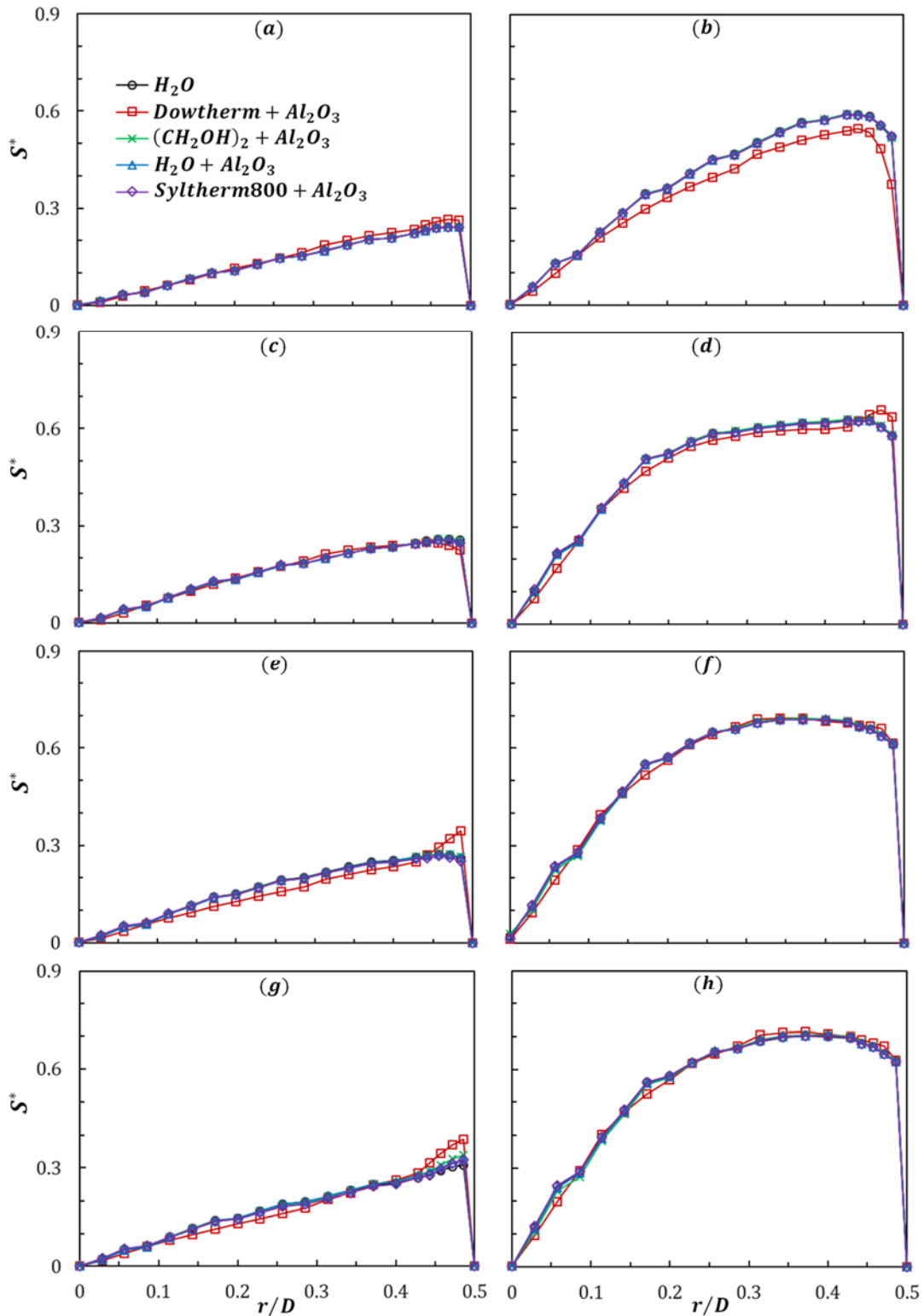
Fig. 10 Radial distributions of Local swirl characteristics of pure water and different nanofluids (φ = 1%) at the nozzle exit plane (x/D = 14.425) at: (a), (b) Re = 5000; (c), (d) Re = 11600; (e), (f) Re = 24600; and (g), (h) Re = 35000 at: (b), (c), (e), (g) Q_r = 0.5; and (b), (d), (f), (g) Q_r = 1.
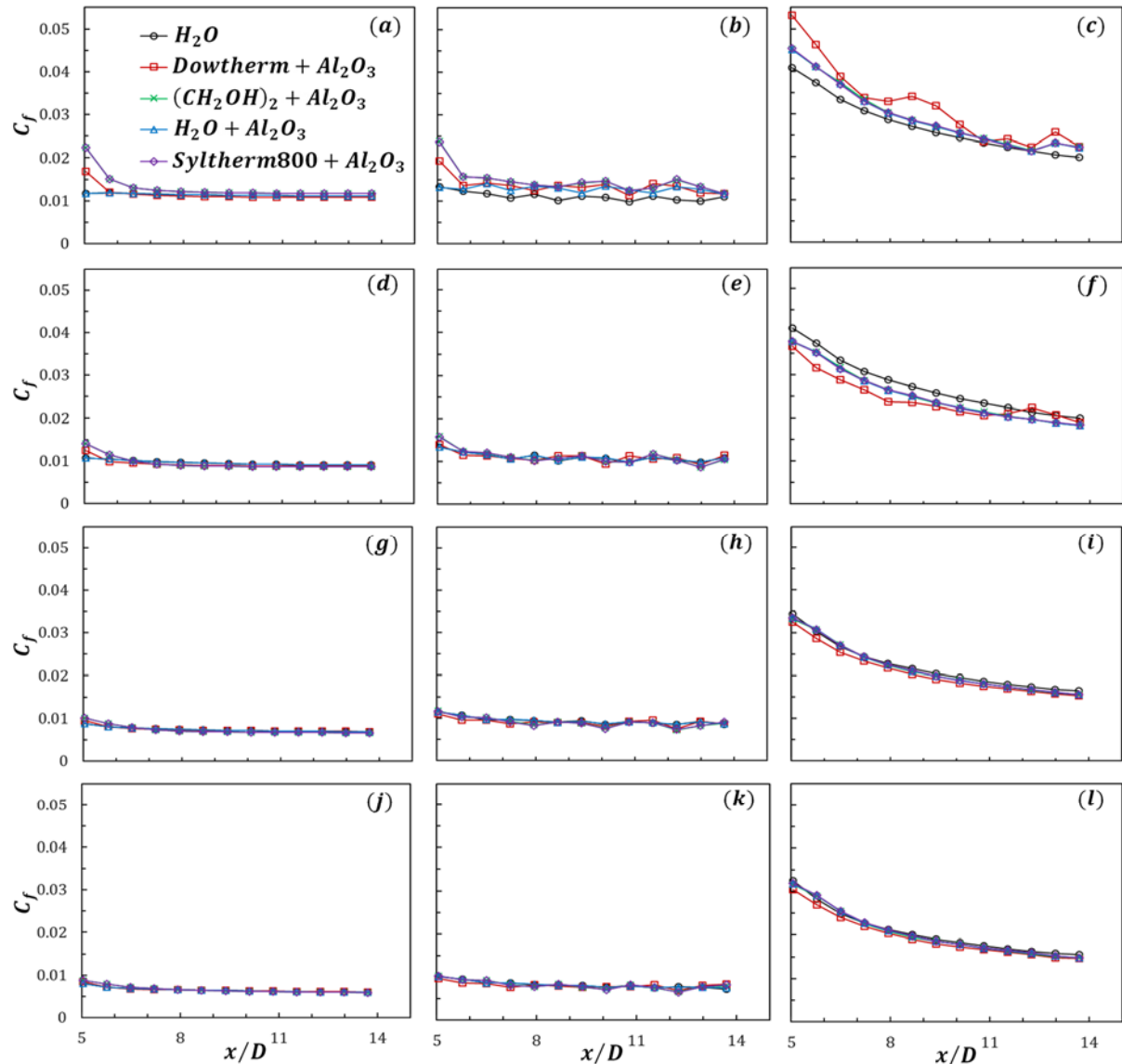
Fig. 11 Axial distributions of skin friction coefficient of pure water and different nanofluids ($\varphi = 1\%$) at: (a), (b), (c) Re = 5000; (d), (e), (f) Re = 11600; (g), (h), (i) Re = 24600; and (j), (k), (l) Re = 35000 at: (a), (d), (g), (h) $Q_r = 0$; (b), (e), (h), (k) $Q_r = 0.5$; and (c), (f), (i), (l) $Q_r = 1$.

3.8 Surface heat transfer coefficient

Fig. 12 describes the surface heat transfer coefficient for water and different nanofluids ($\varphi = 1\%$) for different Reynolds numbers and swirl conditions. The surface heat transfer coefficient is calculated by averaging the data from the different radial locations for the most precise anticipation. It is observed that the surface heat transfer coefficient is increasing with the Reynolds numbers for all the fluids since due to the high Reynolds number the flow velocity as well as the heat transfer rate increases. Moreover, water and aqueous nanofluid exhibit the same characteristics at no swirl ($Q_r = 0$) flow for all the Reynolds numbers. Even for higher Reynolds numbers such as 24600 and 35000 at medium ($Q_r = 0.5$) and high swirl ($Q_r = 1$) conditions the heat transfer coefficient profile tends to merge. However, for low Reynolds numbers, the surface heat transfer coefficient of water is greater than $H_2O + Al_2O_3$ at medium and high swirl cases. This might be attributed to the fact of increased density of $H_2O + Al_2O_3$ [1027.018 kg/m^3] than the pure H_2O [998.2 kg/m^3], which retards the flow and consequently, the heat transfer rate reduces. This behavior is

substantiated by the surface heat transfer coefficient of Syltherm800 + Al_2O_3 and Dowtherm + Al_2O_3 in which the former has a higher heat transfer coefficient and lower density [960.136 kg/m^3] than the latter one [1084.24 kg/m^3]. Obviously, density is not the sole parameter, and in fact, viscosity and thermal conductivity are more dominating parameters than the density itself, which is observed from the heat transfer coefficient of pure H_2O, H_2O + Al_2O_3, and Syltherm800 + Al_2O_3, however, among the nanofluids of nearly equal viscosity and thermal conductivity such as Syltherm800 + Al_2O_3 and Dowtherm + Al_2O_3, the density is predominant. Therefore, the complex combination of the nanofluid effective properties has derived the heat transfer anticipation intricate. Interestingly, the surface heat transfer coefficient of $(CH_2OH)_2$ + Al_2O_3 is significantly high for all the flow conditions [Fig. A4]. It is also observed that for strong swirl flow, the surface heat transfer coefficient near the nozzle inlet is high and gradually decreases with the axial distance.
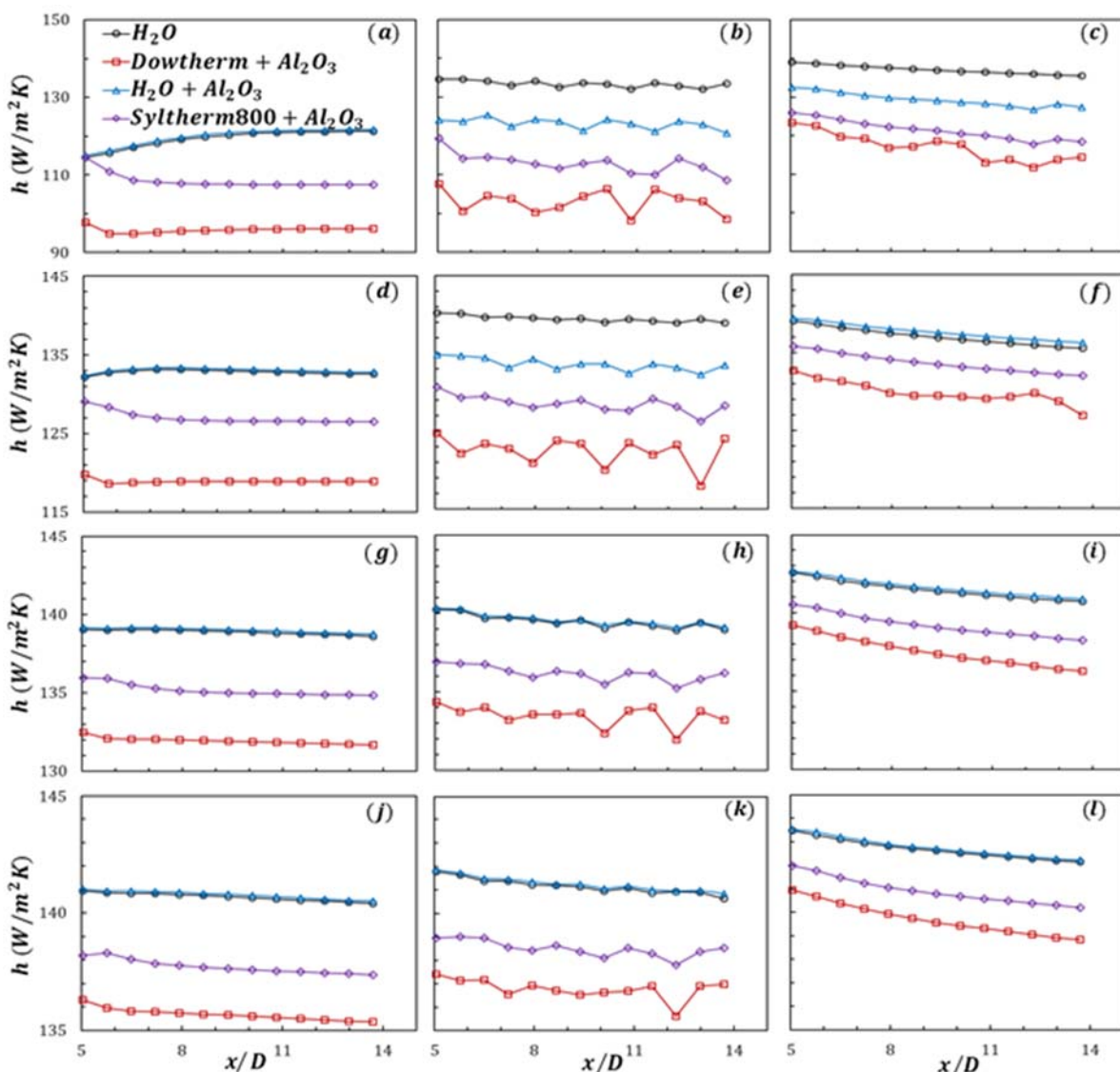

Fig. 12 Axial distributions of surface heat transfer coefficient of pure water and different nanofluids (φ = 1%) at: (a), (b), (c) Re = 5000; (d), (e), (f) Re = 11600; (g), (h), (i) Re = 24600; and (j), (k), (l) Re = 35000 at: (a), (d), (g), (h) Q_r = 0; (b), (e), (h), (k) Q_r = 0.5; and (c), (f), (i), (l) Q_r = 1.
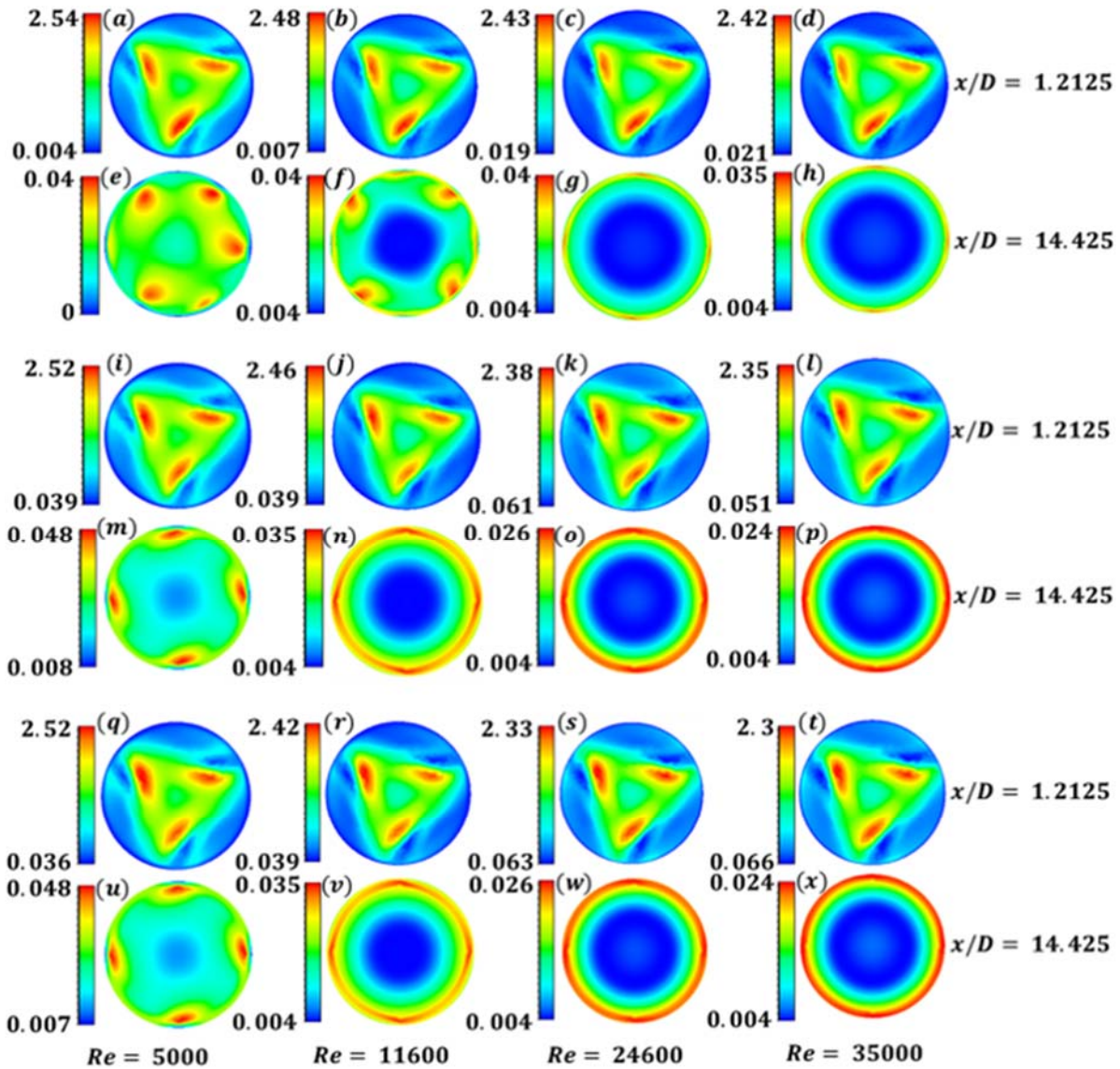
Fig. 13 Non-dimensional turbulent kinetic energy (k/U_b^2) contours for the effect of different non-aqueous nanofluids ($\varphi = 1\%$), namely, (a-h) Dowtherm + Al₂O₃, (i-p) (CH₂OH)₂ + Al₂O₃, (q-x) Syltherm800 + Al₂O₃, for $Q_r = 1$ at different axial positions of the swirling nozzle for different Reynolds numbers. The left-side color legend indicates the value for each contour.

3.9 Turbulent kinetic energy

Fig. 13 presents the contours of normalized turbulent kinetic energy (k/U_b^2) for different non-aqueous nanofluids ($\varphi = 1\%$) at several axial positions of the nozzle for different Reynolds numbers at the strongest swirling condition ($Q_r = 1$). The normalization is done by dividing the turbulent kinetic energies by the square of the corresponding bulk velocities. In general, when the fluid enters the nozzle, the turbulent kinetic energy is very high and maximum for all the nanofluids. Then the turbulent kinetic energy reduces with the axial distance, due to the turbulence and swirl dissipation at the wall. It appears that the turbulent kinetic energy is lower at the nozzle center than the wall vicinity at the nozzle exit (x/D = 14.425). This is because, at higher swirling conditions, the flow is intense in the outer half of the nozzle due to the centrifugal forces associated with swirling flow. However, in the case of low Reynolds numbers, an exception of this

20

phenomenon is observed for all the nanofluids. It is also evident that the turbulent kinetic energy is reducing with increasing Reynolds number since the flow velocity increases. Besides, Dowtherm + Al_2O_3 predicts the maximum turbulent kinetic energy among the nanofluids. The low viscosity of Dowtherm + Al_2O_3 might be attributed to this high turbulence kinetic energy. When the viscosity is high the fluid becomes sticky which restricts the proper fluid flow. Instead, relatively low viscous fluid can freely move and generate extensive turbulence.

4. Conclusion

Incompressible turbulent low concentration (φ = 1%) aqueous and non-aqueous nanofluids flow through a heated aerodynamic swirl nozzle is investigated numerically in this study. An axial-plus-tangential flow is considered for seamless transitions from non-swirl ($Q_r = 0$) to high swirl ($Q_r = 1$) generation. Finite volume-based commercial software ANSYS Fluent v17 is used in the simulation to investigate the mechanical and thermal characteristics. Governing equations are approximated by the RANS and energy equations, whereby turbulence is characterized by the Realizable k-ε model. The study examined various flow and thermal parameters for several nanofluids at three different swirl conditions ($Q_r = 0$, $Q_r = 0.5$, and $Q_r = 1$) and four different Reynolds numbers (Re = 5000, Re = 11600, Re = 24600, and Re = 35000). A compendium of the outcomes is given below:

- Aqueous nanofluid exhibits the property of water in terms of thermal and mechanical behavior since the concentration of nanoparticles is low. The thermofluidic behavior of the non-aqueous nanofluids differs significantly from the aqueous nanofluids.

- The non-aqueous nanofluids show higher average Nusselt numbers than the aqueous nanofluids from no swirl to high swirl cases. The average Nusselt number increases up to 322% for Dowtherm + Al_2O_3 and 320% for Syltherm800 + Al_2O_3 compared to H_2O. Besides, the average Nusselt number of $(CH_2OH)_2$ + Al_2O_3 is significantly higher than the other nanofluids.

- The pressure drop is directly proportional to the effective viscosity of the nanofluids since the stickiness of the fluid that results in friction increases with viscosity. In general, the pressure drop of the non-aqueous nanofluids is higher than the aqueous nanofluids.

- The thermal performance factor of the aqueous nanofluid is greater than the non-aqueous nanofluids due to the high thermal conductivity as well as the low viscosity. Moreover, the thermal performance factor is independent of the Reynolds number of almost all the nanofluids except the $(CH_2OH)_2$ + Al_2O_3.

- The skin friction coefficients at no swirl and medium swirl flow exhibit the same behavior for all the nanofluids and are comparatively lower than for high swirl cases. The skin friction coefficient decreases with the Reynolds number, especially for the high swirl cases.

- The turbulent kinetic energy is the maximum at the nozzle inlet and reduces with the axial distance. Moreover, the near-wall turbulent kinetic energy is higher than the nozzle center at the nozzle exit plane.

- Correlations are established for the average Nusselt number and thermal performance factor of nanofluids.

References

[1] Al-Abdeli, Y. M., & Masri, A. R. (2003). Recirculation and flowfield regimes of unconfined non-reacting swirling flows. Experimental Thermal and Fluid Science, 27(5), 655-665.

[2] Toh, I. K., Honnery, D., & Soria, J. (2010). Axial plus tangential entry swirling jet. Experiments in Fluids 48 (2): 309–325. doi:10.1007/s00348-009-0734-2.

[3] Rose, W. G. (1962). A swirling round turbulent jet: 1—Mean-Flow measurements. Journal of Applied Mechanics 29 (4): 615–625. doi:10.1115/1.3640644.

[4] Jafari, M., Farhadi, M., & Sedighi, K. (2017). An experimental study on the effects of a new swirl generator on thermal performance of a circular tube. International Communications in Heat and Mass Transfer, 87, 277-287.

[5] Gore, R. W., and Ranz, W. E. (1964).

"Backflows in Rotating Fluids Moving Axially through Expanding Cross Sections." AIChE Journal 10 (1): 83–88. doi:10.1002/aic.690100126.

[6] Felli, M., Falchi, M., & Fornari, P. (2008). Impinging swirling jet against a wall: experimental investigation by PIV and high speed visualizations. Propulsion and Cavitation Laboratory, INSEAN, Italy.

[7] Al-Abdeli, Y. M., & Masri, A. R. (2004). Precession and recirculation in turbulent swirling isothermal jets. Combustion Science and Technology 176 (5–6): 645–665. doi:10.1080/00102200490427883.

[8] Markal, B. (2018). Experimental investigation of heat transfer characteristics and wall pressure distribution of swirling coaxial confined impinging air jets, International Journal of Heat and Mass Transfer. 124, pp.517–532.

[9] Ahmed, Z.U. (2016) An Experimental and Numerical Study of Surface Interactions in Turbulent Swirling Jets, PhD thesis, Edith Cowan University, Australia.

[10] Heris, S. Z., Edalati, Z., Noie, S. H., & Mahian, O. (2014). Experimental investigation of Al_2O_3/water nanofluid through equilateral triangular duct with constant wall heat flux in laminar flow. Heat Transfer Engineering, 35(13), 1173-1182.

[11] Heris, S. Z., Nassan, T. H., Noie, S. H., Sardarabadi, H., & Sardarabadi, M. (2013). Laminar convective heat transfer of Al_2O_3/water nanofluid through square cross-sectional duct. International Journal of Heat and Fluid Flow, 44, 375-382.

[12] Sözen, A., Gürü, M., Khanlari, A., & Çiftçi, E. (2019). Experimental and numerical study on enhancement of heat transfer characteristics of a heat pipe utilizing aqueous clinoptilolite nanofluid. Applied Thermal Engineering 160: 114001. doi:10.1016/j.applthermaleng.2019.114001.

[13] Mohammed, H. A., & Narrein, K. (2012). Thermal and hydraulic characteristics of nanofluid flow in a helically coiled tube heat exchanger. International Communications in Heat and Mass Transfer 39 (9): 1375–1383. doi:10.1016/j.icheatmasstransfer. 2012.07.019.

[14] Khanlari, A., Sözen, A., & Variyenli, H. İ. (2019). Simulation and experimental analysis of heat transfer characteristics in the plate type heat exchangers using TiO2/water nanofluid. International Journal of Numerical Methods for Heat & Fluid Flow 29 (4): 1343–1362. doi:10.1108/HFF-05-2018-0191.

[15] Moghadam, A. J., Farzane-Gord, M., Sajadi, M., & Hoseyn-Zadeh, M. (2014). Effects of CuO/water nanofluid on the efficiency of a flat-plate solar collector. Experimental Thermal and Fluid Science 58: 9–14. doi:10.1016/ j.expthermflusci.2014.06.014.

[16] Hoseinzadeh, S., Sahebi, S. A. R., Ghasemiasl, R., & Majidian, A. R. (2017). Experimental analysis to improving thermosyphon (TPCT) thermal efficiency using nanoparticles/based fluids (Water). The European Physical Journal Plus 132 (5): 197. doi:10.1140/epjp/i2017-11455-3.

[17] Nazari, M. A., Ghasempour, R., Ahmadi, M. H., Heydarian, G., & Shafii, M. B. (2018). Experimental investigation of graphene oxide nanofluid on heat transfer enhancement of pulsating heat pipe. International Communications in Heat and Mass Transfer 91: 90–94. doi:10.1016/ j.icheatmasstransfer. 2017.12.006.

[18] Karimi, Y., Nazar, A. R. S., & Motevasel, M. (2020). CFD simulation of nanofluid heat transfer considering the aggregation of nanoparticles in population balance model. Journal of Thermal Analysis and Calorimetry, 1-14.

[19] Kahani, M., Heris, S. Z., & Mousavi, S. M. (2013). Effects of curvature ratio and coil pitch spacing on heat transfer performance of Al_2O_3/water nanofluid laminar flow through helical coils. Journal of Dispersion Science and Technology, 34(12), 1704-1712.

[20] Pandey, S. D., & Nema, V. K. (2012). Experimental analysis of heat transfer and friction factor of nanofluid as a coolant in a corrugated plate heat exchanger. Experimental Thermal and Fluid Science, 38, 248-256.

[21] Azmi, W. H., Sharma, K. V., Sarma, P. K., Mamat, R., Anuar, S., & Sundar, L. S. (2014). Numerical validation of experimental heat transfer coefficient with SiO_2 nanofluid flowing in a tube with twisted tape inserts. Applied Thermal Engineering, 73(1), 296-306.

[22] Fotukian, S. M., & Esfahany, M. N. (2010). Experimental investigation of turbulent convective heat transfer of dilute γ-Al_2O_3/water nanofluid inside a circular tube. International Journal of Heat & Fluid Flow 31 (4): 606–612. doi:10.1016/j. ijheatfluidflow. 2010.02.020.

[23] Naphon, P., Assadamongkol, P., & Borirak, T. (2008). Experimental investigation of titanium nanofluids on the heat pipe thermal efficiency. International Communications in Heat and Mass Transfer 35 (10): 1316–1319. doi:10.1016/j.icheatmasstransfer.2008.07.010.

[24] Sajadi, A. R., & Kazemi, M. H. (2011).

Investigation of turbulent convective heat transfer and pressure drop of TiO$_2$/water nanofluid in circular tube. International Communications in Heat and Mass Transfer 38 (10): 1474–1478. doi:10.1016/j.icheatmass transfer.2011.07.007.

[25] Islam, S. M., Khan, M. T. & Ahmed, Z. U. (2020). Effect of design parameters on flow characteristics of an aerodynamic swirl nozzle. Progress in Computational Fluid Dynamics, 20(5), 249–262.

[26] Halder, M. R., S. K. Dash, and S. K. Som (2003), "Influences of Nozzle Flow and Nozzle Geometry on the Shape and Size of an Air Core in a Hollow Cone Swirl Nozzle," Proceedings of the Institution of Mechanical Engineers, Part C: Journal of Mechanical Engineering Science, 217(2), 207–217. doi:10.1243/095440603762826521.

[27] Promvonge, P., and S. Eiamsa-Ard. 2006. "Heat Transfer Enhancement in a Tube with Combined Conical-nozzle Inserts and Swirl Generator." Energy Conversion and Management 47 (18–19): 2867–2882. doi:10.1016/j. enconman.2006.03.034.

[28] Singh, N. K., and K. Ramamurthi. 2009. "Formation of Coanda Jet from Sharp-edged Swirl Nozzle with Base Plate." Experimental Thermal and Fluid Science 33 (4): 675–682. doi:10.1016/j.expthermflusci.2009.01.008.

[29] Khan, M. T., S. M. Islam, and Z. U. Ahmed. 2020. "Near- wall and Turbulence Behavior of Swirl Flows through an Aerodynamic Nozzle." Journal of Engineering Advancements 1 (2): 43–52. doi:10.38032/jea.2020.02.003.

[30] Guo, H. F., Z. Y. Chen, and C. W. Yu. 2009. "3D Numerical Simulation of Compressible Swirling Flow Induced by Means of Tangential Inlets." International Journal for Numerical Methods in Fluids 59 (11): 1285–1298. doi:10.1002/fld.1872.

[31] Hreiz, R., C. Gentric, and N. Midoux. 2011. "Numerical Investigation of Swirling Flow in Cylindrical Cyclones." Chemical Engineering Research and Design 89 (12): 2521–2539. doi:10.1016/j.cherd.2011.05.001.

[32] Najafi, A. F., M. H. Saidi, M. S. Sadeghipour, and M. Souhar. 2005. "Numerical Analysis of Turbulent Swirling Decay Pipe Flow." International Communications in Heat and Mass Transfer 32 (5): 627–638. doi:10.1016/j. icheatmasstransfer.2004.10.014.

[33] Sentyabov, A. V., A. A. Gavrilov, and A. A. Dekterev. 2011. "Investigation of Turbulence Models for Computation of Swirling Flows." Thermophysics and Aeromechanics 18 (1): 73. doi:10.1134/S0869864311010094.

[34] Escue, A., and J. Cui. 2010. "Comparison of Turbulence Models in Simulating Swirling Pipe Flows." Applied Mathematical Modelling 34 (10): 2840–2849. doi:10.1016/j.apm.2009.12.018.

[35] Saqr, K. M., and M. A. Wahid. 2014. "Effects of Swirl Intensity on Heat Transfer and Entropy Generation in Turbulent Decaying Swirl Flow." Applied Thermal Engineering 70 (1): 486–493. doi:10.1016/j.applthermaleng.2014.05.059.

[36] Akyürek, E. F., K. Geliş, B. Şahin, and E. Manay. 2018. "Experimental Analysis for Heat Transfer of Nanofluid with Wire Coil Turbulators in a Concentric Tube Heat Exchanger." Results in Physics 9: 376–389. doi:10.1016/j. rinp.2018.02.067.

[37] Kanti, P. K., Sharma, K. V., Minea, A. A., & Kesti, V. (2021). Experimental and computational determination of heat transfer, entropy generation and pressure drop under turbulent flow in a tube with fly ash-Cu hybrid nanofluid. International Journal of Thermal Sciences, 167, 107016.

[38] Reddy, M. C. S., and V. V. Rao. 2014. "Experimental Investigation of Heat Transfer Coefficient and Friction Factor of Ethylene Glycol Water Based TiO$_2$ Nanofluid in Double Pipe Heat Exchanger with and without Helical Coil Inserts." International Communications in Heat and Mass Transfer 50: 68–76. doi:10.1016/j.icheatmasstransfer. 2013.11.002.

[39] Kahani, M., Heris, S. Z., & Mousavi, S. M. (2013). Comparative study between metal oxide nanopowders on thermal characteristics of nanofluid flow through helical coils. Powder technology, 246, 82-92.

[40] Kahani, M., Zeinali Heris, S., & Mousavi, S. M. (2014). Experimental investigation of TiO$_2$/water nanofluid laminar forced convective heat transfer through helical coiled tube. Heat and Mass Transfer, 50, 1563-1573.

[41] Zeinali Heris, S., Noie, S. H., Talaii, E., & Sargolzaei, J. (2011). Numerical investigation of Al$_2$O$_3$/water nanofluid laminar convective heat transfer through triangular ducts. Nanoscale research letters, 6, 1-10.

[42] Zeinali Heris, S., Kazemi-Beydokhti, A., Noie, S. H., & Rezvan, S. (2012). Numerical study on convective heat transfer of Al$_2$O$_3$/water, CuO/water and Cu/water nanofluids through square cross-section duct in laminar flow. Engineering Applications of Computational Fluid Mechanics, 6(1), 1-14.

[43] Asmaie, L., M. Haghshenasfard, A. Mehrabani-Zeinabad, and M. N. Esfahany. 2013. "Thermal Performance Analysis of

Nanofluids in a Thermosyphon Heat Pipe Using CFD Modeling." Heat and Mass Transfer 49 (5): 667–678. doi:10.1007/s00231-013-1110-6.

[44] Choi, J., and Y. Zhang. 2012. "Numerical Simulation of Laminar Forced Convection Heat Transfer of Al_2O_3– water Nanofluid in a Pipe with Return Bend." International Journal of Thermal Sciences 55: 90–102. doi:10.1016/j.ijthermalsci.2011.12.017.

[45] Wanatasanappan, V. V., Kanti, P. K., Sharma, P., Husna, N., & Abdullah, M. Z. (2023). Viscosity and rheological behavior of Al_2O_3-Fe_2O_3/water-EG based hybrid nanofluid: A new correlation based on mixture ratio. Journal of Molecular Liquids, 375, 121365.

[46] Behroyan, I., S. M. Vanaki, P. Ganesan, and R. Saidur. 2016. "A Comprehensive Comparison of Various CFD Models for Convective Heat Transfer of Al_2O_3 Nanofluid inside A Heated Tube." International Communications in Heat and Mass Transfer 70: 27–37. doi:10.1016/j.icheatmasstransfer.2015.11.001.

[47] Meng, X., and Y. Li. 2015. "Numerical Study of Natural Convection in a Horizontal Cylinder Filled with Water-based Alumina Nanofluid." Nanoscale Research Letters 10 (1): 142. doi:10.1186/s11671-015-0847-x.

[48] Shirvan, K. M., M. Mamourian, S. Mirzakhanlari, and R. Ellahi. 2017. "Numerical Investigation of Heat Exchanger Effectiveness in a Double Pipe Heat Exchanger Filled with Nanofluid: A Sensitivity Analysis by Response Surface Methodology." Powder Technology 313: 99–111. doi:10.1016/j.powtec.2017.02.065.

[49] Purohit, N., V. A. Purohit, and K. Purohit. 2016. "Assessment of Nanofluids for Laminar Convective Heat Transfer: A Numerical Study." Engineering Science and Technology, an International Journal 19 (1): 574–586. doi:10.1016/j.jestch.2015.08.010.

[50] Solomon, A. B., K. Ramachandran, L. G. Asirvatham, and B. C. Pillai. 2014. "Numerical Analysis of a Screen Mesh Wick Heat Pipe with Cu/water Nanofluid." International Journal of Heat and Mass Transfer 75: 523–533. doi:10.1016/j.ijheatmasstransfer.2014.04.007.

[51] Khan, T., & Ahmed, Z. U. (2022). Effect of nanofluids on heat transfer characteristics of an aerodynamic swirl nozzle for isothermal and isoflux conditions. Australian Journal of Mechanical Engineering, 1-19. doi: 10.1080/14484846.2022.2066837.

[52] Debnath, S., Khan, T. & Ahmed, Z. U., Substrate Characteristics of Multiple Arrays

of Turbulent Swirling Impinging Jets, Journal of Flow Visualization & Image Processing 30(4):67–96 (2023).

[53] T.H. Shih, W.W.Liou, A.Shabbir, Z.Yang,Z. & J.Zhu, "A New k-ε Eddy-Viscosity Model for High Reynolds Number Turbulent Flows - Model Development and Validation. Computers Fluids, 24(3):227-238, (1995).

[54] ANSYS, Inc. (2020). ANSYS Fluent Theory Guide 2020 R1.

[55] Ahmed, Z. U., Raihan, M. R., Ghaffari, O., & Ikhlaq, M. (2022). Thermal and Hydraulic Performances of Porous Microchannel Heat Sink using Nanofluids. Journal of Thermal Science and Engineering Applications, 14(7), 071012.

[56] Xuan, Y., and Roetzel, W. (2000), Conceptions for heat transfer correlation of nanofluids, International Journal of Heat and Mass Transfer, 43(19), 3701-3707.

[57] Nasrin, R., Alim, M. A., and Chamkha, A. J. (2012), Buoyancy-driven heat transfer of water– Al_2O_3 nanofluid in a closed chamber: Effects of solid volume fraction, Prandtl number and aspect ratio, International Journal of Heat and Mass Transfer, 55(25-26), 7355-7365.

[58] Maxwell-Garnett, J. C. (1904), Colours in metal glasses and in metallic films. Phil. Trans. R. Soc. Lond, A, 203, 385-420.

[59] Brinkman, H. C. (1952), The viscosity of concentrated suspensions and solutions, The Journal of Chemical Physics, 20(4), 571-571.

[60] Murshed, S. S., & de Castro, C. N. (2016). Conduction and convection heat transfer characteristics of ethylene glycol based nanofluids–a review. Applied energy, 184, 681-695.

[61] Y. Ding, H. Alias, D. Wen, R.A. Williams, Heat transfer of aqueous suspensions of carbon nanotubes (CNT nanofluids), International Journal of Heat and Mass Transfer 49 (1–2) (2005) 240–250.

[62] N. Putra, W. Roetzel, S.K. Das, Natural convection of nano-fluids, Heat and Mass Transfer 39 (8–9) (2003) 775–784.

[63] Kanti, P., Sharma, K. V., Said, Z., & Bellos, E. (2022). Numerical study on the thermo-hydraulic performance analysis of fly ash nanofluid. Journal of Thermal Analysis and Calorimetry, 147(3), 2101-2113.

[64] Debnath, S., Ahmed, Z. U., Ikhlaq, M., & Khan, T. (2023). Thermal characteristics of arrays of swirling impinging jets: Effect of Reynolds number, impingement distance, and jet‐to‐jet separation. Heat Transfer, 52(1),

585-608.

[65] Debnath, S., Khan, M. T., & Ahmed, Z. U. (2022). Investigation on Circular Array of Turbulent Impinging Round Jets at Confined Case: A CFD Study. Journal of Engineering Advancements, 3(04), 144-154.

[66] Khan, T., Debnath, S., Ahmed, Z. U., & Islam, S.M. Effects of impinging distance, Reynolds number, and swirl on the flow and heat transfer behaviors of arrays of circular impinging jets: A numerical approach. International Conference on Mechanical, Industrial and Energy Engineering 2022 (ICMIEE-2022).

[67] Khan, M. H. U., & Ahmed, Z. U. (2019). Fluid flow and heat transfer characteristics of multiple swirling impinging jets at various impingement distances. International Journal of Thermofluid Science and Technology, 6(4), 19060403. doi.org/10.36963/ IJTST.19060403.

[68] Azmi, W. H., K. V. Sharma, P. K. Sarma, R. Mamat, S. Anuar, and V. D. Rao. 2013. "Experimental Determination of Turbulent Forced Convection Heat Transfer and Friction Factor with SiO_2 Nanofluid." Experimental Thermal and Fluid Science 51: 103–111. doi:10.1016/j.expthermflusci.2013.07.006.

[69] Sekrani, G., & Poncet, S. (2018). Ethylene- and propylene-glycol based nanofluids: a litterature review on their thermophysical properties and thermal performances. Applied Sciences, 8(11), 2311. doi:10.3390/app8112311

[70] Dowtherm, A. (1997), "Heat Transfer Fluid, Product Technical Data."

[71] Mwesigye, A., Z. Huan, and J. P. Meyer. 2015. "Thermodynamic Optimisation of the Performance of a Parabolic Trough Receiver Using Synthetic oil–Al_2O_3 Nanofluid." Applied Energy 156: 398–412. doi:10.1016/j. apenergy.2015.07.035.
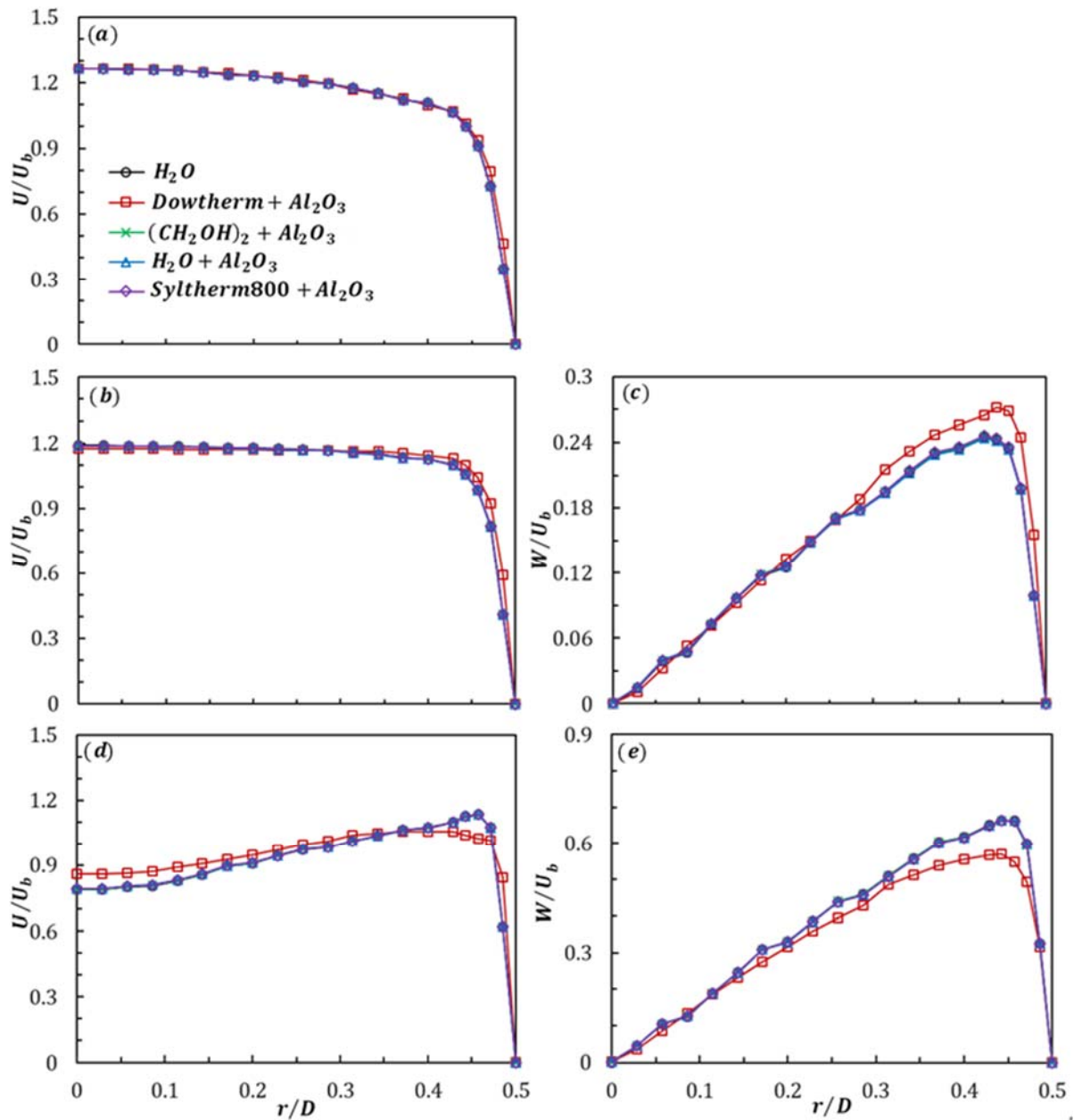
Appendix

Fig. A1 Radial distributions of normalised (a), (b), (d) axial (U/U_b) and (c), (e) tangential (W/U_b) velocities of different nanofluids ($\varphi = 1\%$) along with water at the nozzle exit plane (x/D = 14.425) for Re = 5000 at: (a) $Q_r = 0$, (b), (c) $Q_r = 0.5$, and (d), (e) $Q_r = 1$.
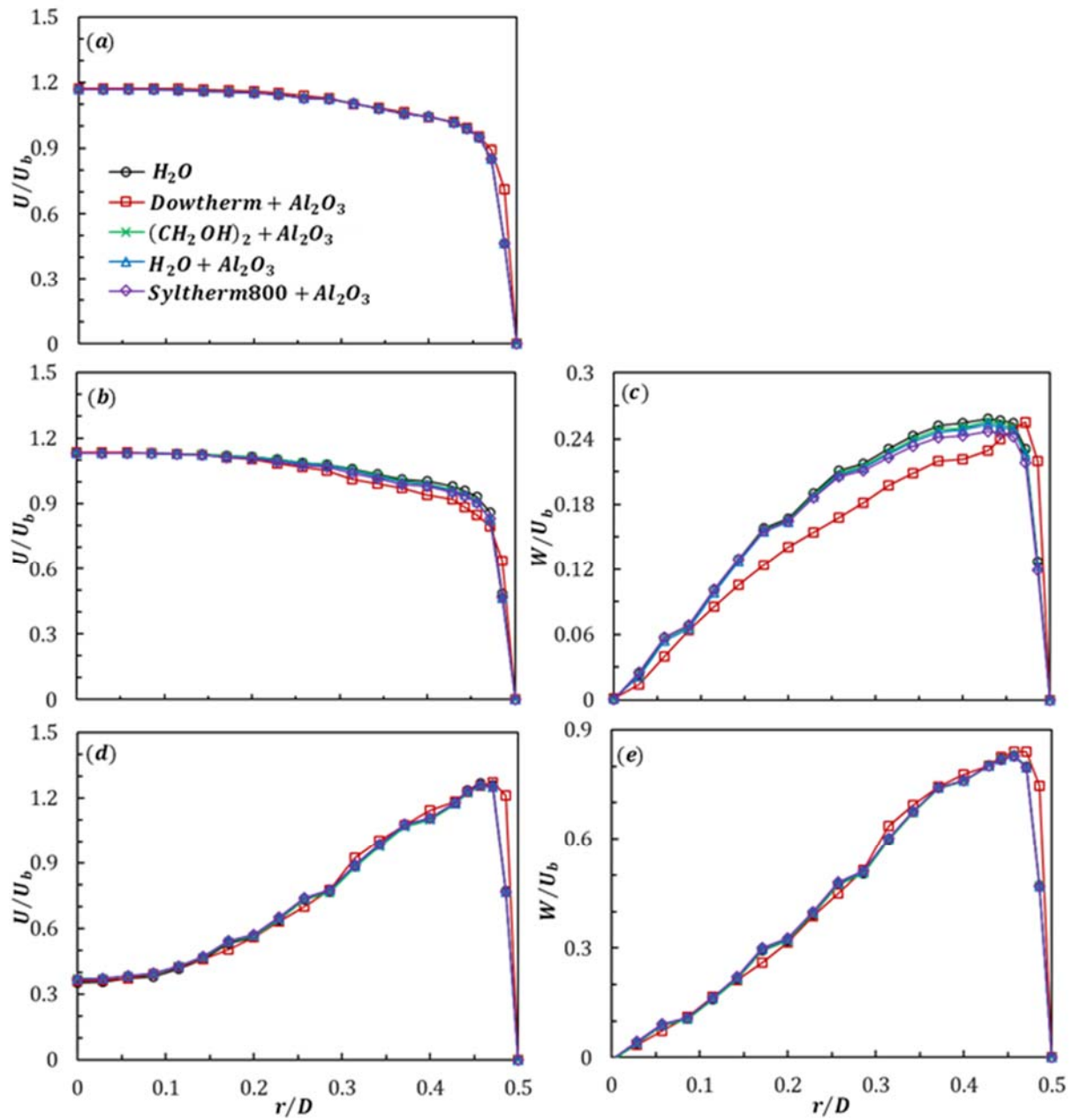
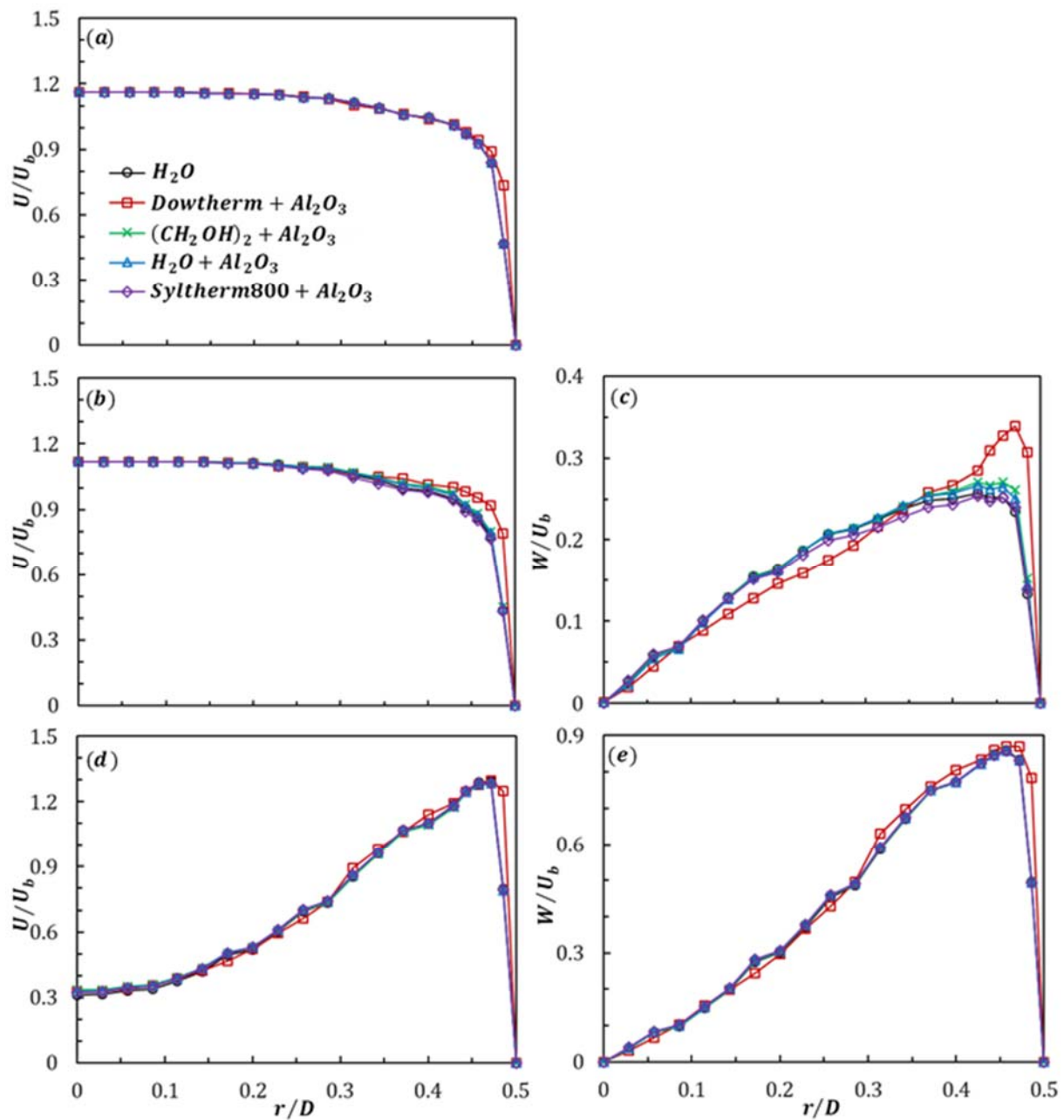Fig. A2 Radial distributions of normalised (a), (b), (d) axial (U/U_b) and (c), (e) tangential (W/U_b) velocities of different nanofluids ($\varphi = 1\%$) along with water at the nozzle exit plane (x/D = 14.425) for Re = 24,600 at: (a) $Q_r = 0$, (b), (c) $Q_r = 0.5$, and (d), (e) $Q_r = 1$.

Fig. A3 Radial distributions of normalised (a), (b), (d) axial (U/U_b) and (c), (e) tangential (W/U_b) velocities of different nanofluids ($\varphi = 1\%$) along with water at the nozzle exit plane ($x/D = 14.425$) for Re = 35,000 at: (a) $Q_r = 0$, (b), (c) $Q_r = 0.5$, and (d), (e) $Q_r = 1$.
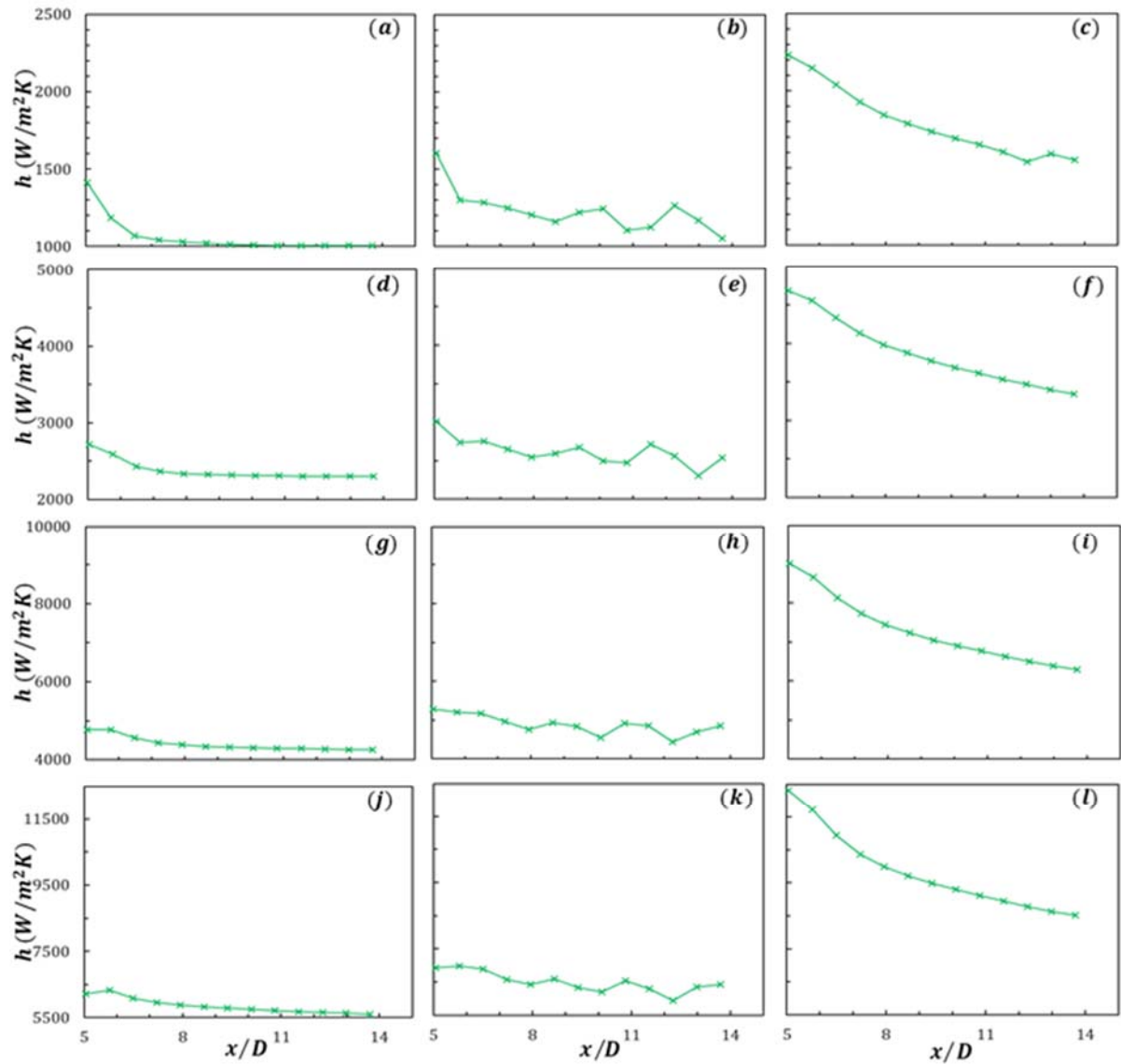
Fig. A4 Axial distributions of surface heat transfer coefficients of $(CH_2OH)_2 + Al_2O_3$ ($\varphi = 1\%$) at: (a), (b), (c) Re = 5000; (d), (e), (f) Re = 11600; (g), (h), (i) Re = 24600; and (j), (k), (l) Re = 35000 at: (a), (d), (g), (h) $Q_r = 0$; (b), (e), (h), (k) $Q_r = 0.5$; and (c), (f), (i), (l) $Q_r = 1$.